MNRAS **000**, 1–19 (2017) Preprint 14 November 2018 Compiled using MNRAS LATEX style file v3.0

The NGC 454 system: anatomy of a mixed on-going merger⋆

H. Plana[1],† R. Rampazzo[2], P. Mazzei[2], A. Marino[2], Ph. Amram[3], A.L.B. Ribeiro[1]
[1]*Laboratório de Astrofísica Teórica e Observational, Universidade Estadual de Santa Cruz – 45650-000 Ilhéus - Bahia Brazil*
[2]*INAF-Osservatorio Astronomico di Padova, Vicolo dell'Osservatorio 5, 35122 Padova Italy*
[3]*Aix Marseille Univ., CNRS, Laboratoire d'Astrophysique de Marseille (LAM) 38 rue Frédéric Joliot-Curie F-13388 Marseille Cedex 13 France*

Accepted XXX. Received YYY; in original form ZZZ

ABSTRACT

This paper focuses on NGC 454, a nearby interacting pair of galaxies (AM0112-554, RR23), composed of an early-type (NGC 454 E) and a star forming late-type companion (NGC 454 W). We aim at characterizing this wet merger candidate via a multi-λ analysis, from near-UV to optical using SWIFT–UVOT, and mapping the Hα intensity (I) distribution, velocity (V_r), and velocity dispersion (σ) fields with SAM+Perot-Fabry@SOAR observations. Luminosity profiles suggest that NGC 454 E is an S0. Distortions in its outskirts caused by the on-going interaction are visible in both optical and near-UV frames. In NGC 454 W, the NUV-UVOT images and the Hα show a set of star forming complexes connected by a faint tail. Hα emission is detected along the line connecting NGC 454 E to the NGC 454 main H II complex. We investigate the $(I-\sigma)$, $(I-V_r)$ $(V_r-\sigma)$ diagnostic diagrams of the H II complexes, most of which can be interpreted in a framework of expanding bubbles. In the main H II complex, enclosed in the UV brightest region, the gas velocity dispersion is highly supersonic reaching 60 km s^{-1}. However, Hα emission profiles are mostly asymmetric indicating the presence of multiple components with an irregular kinematics. Observations point towards an advanced stage of the encounter. Our SPH simulations with chemo-photometric implementation suggest that this mixed pair can be understood in terms of a 1:1 gas/halos encounter giving rise to a merger in about 0.2 Gyr from the present stage.

Key words: Galaxies — interactions; galaxies: elliptical and lenticular, cD; galaxies: irregular; galaxies: kinematics and dynamics; galaxies: photometry

1 INTRODUCTION

Interactions modify the gravitational potential of the involved galaxies and may lead to their merger. During the interaction the stellar and gas components of each galaxy respond differently to the potential variation. The outcome is directly measurable in terms of morphology, kinematics and, in general, of the physical properties of each galaxy, such as their star formation rate and AGN activity. A comprehensive description of the *job of interactions* in shaping galaxies and their properties as investigated in last decades of extragalactic research is widely presented and discussed by Struck (2011, and references therein).

Pairs of galaxies have been used as probes to study interactions. Well-selected samples of pairs and catalogues have been produced (see e.g. Karachentsev 1972; Peterson 1979; Rampazzo et al. 1995; Soares et al. 1995; Barton 2000). Single studies as well as surveys of pair catalogues have been crucial to reveal several interaction effects once compared to isolated/unperturbed galaxy samples (see e.g. Rampazzo et al. 2016, Section 5.3.2).

Although the vast majority of pair members have similar morphological types, a first light on the existence of mixed morphology pairs has been shed by the Karachentsev (1972) Catalog of Isolated Pairs. Rampazzo & Sulentic (1992) estimated that between as much as 10-25% of the pairs in any complete (non-hierarchical) sample will be of the mixed morphology type. At the beginning of 1990s, studies about this kind of pairs were addressed to ascertain possible enhancement of the star formation activity, with respect

⋆ Based on observations obtained at the Southern Astrophysical Research (SOAR) telescope, which is a joint project of the Ministério da Ciência, Tecnologia, e Inovação (MCTI) da República Federativa do Brasil, the U.S. National Optical Astronomy Observatory (NOAO), the University of North Carolina at Chapel Hill (UNC), and Michigan State University (MSU).

† E-mail: plana@uesc.br

to non interacting samples, via mid and far infrared observations, at that time often hampered by a low resolution (see e.g. Xu & Sulentic 1991; Surace 1993). Mixed morphology pairs have been thought as the cleanest systems where to verify possible mass transfer between the gas rich and the gas poor member, typically the early-type companion. Several candidates of mixed morphology pairs with star formation and AGN activity, fueled by gas transfer between components, have been indicated (see e.g. de Mello et al. 1995; Rampazzo et al. 1995; deMello et al. 1996; Domingue et al. 2003). The literature reports in general a star formation enhancement in wet and mixed pairs (see e. g. Larson & Tinsley 1978; Combes et al. 1994; Barton 2000; Barton et al. 2003; Smith et al 2007; Knapen & Querejeta 2015; Smith et al. 2016).

The fate of mixed, gravitationally bound pairs is to merge, the available gas may trigger star formation for some time, but it is still unclear what will be the merger product. The role of mixed merger has been investigated by Lin et al. (2008) who suggested that roughly 36% of the present day red galaxies, typically early-type galaxies, have experienced a mixed merger. According to these authors mixed (and wet) mergers will produce red galaxies of intermediate mass, after the quenching of the star formation, while the more massive part of the red sequence should be generated by stellar mass growth via dry-mergers (VanDokkum 2005; Faber et al. 2007).

In the context of star formation, the dynamics of the (ionized, neutral and molecular) gas clouds during interaction is a crucial topic. H I bridges as well as clouds larger than 10^8 $M_\odot$ are detected in wet interacting/merging pairs with 20-40 km s^{-1} velocity dispersion (see e.g. Elmegreen et al. 1993; Irwin 1994; Elmegreen et al. 1995). External gas high velocity dispersion is possibly linked to an internal high velocity dispersion of the clouds, increasing the star formation efficiency. Combes et al. (1994) suggest that the enhancement of the star formation in wet interacting galaxies may be connected to an increase of the molecular gas that inflows toward the center by tidal torque. There are indication that the brightness distribution of H II regions in interacting objects differs from unperturbed ones. Bright H II regions can form by gas flows during interaction. They are on the average brighter than in isolated galaxies and have a high internal velocity dispersion (15-20 km s^{-1}) as reported by Zaragoza-Cardiel et al. (2015). Furthermore, the number of H II regions in interacting objects is bigger than in an isolated galaxies with the same absolute magnitude, suggesting that interactions do in fact increase the star formation rate.

The subject of the present study is the NGC 454 system, a strongly peculiar, interacting (AM 0112-554; Arp & Madore 1987) and isolated Reduzzi & Rampazzo (RR23; 1995) pair in the Southern Hemisphere. Johansson (1988) described the system as "a pair of emission-line galaxies in close interaction, or in the early-stage of a merger, consisting of a large elliptical and a blue irregular galaxy". Figure 1 dissects the system according the regions labeled by Johansson (1988) and Stiavelli et al. (1998). We will adopt their definition along this paper adding the prefix NGC 454.

The East part of the system, (labeled E in Figure 1, NGC 454 E hereafter), identifies the early-type member of the pair. NGC 454 E is crossed by dust lanes and it is distorted by the interaction. The U, B, V Johnson and Gunn I photometry by Johansson (1988) presented the East member as a red elliptical with a luminosity profile that follows closely an $r^{1/4}$ law (de Vaucouleurs 1948) out to 15″ from the galaxy center. The Stiavelli et al. (1998) high resolution HST imaging, in the F450W, F606W, and F814W filters, shows that NGC 454 E is likely an S0. Their luminosity profile, extending out to $\simeq$ 30″, is much better fitted by two components: an $r^{1/4}$ law describing the bulge plus an exponential law (Freeman 1970) for a disk. The (B-V) color profile indicates that the central part of the galaxy, i.e. r$\leq$1″, is red with 1$\lesssim$ (B-V) $\lesssim$1.4 while the outside region is slightly bluer with 0.8$\lesssim$ (B-V) $\lesssim$1. The nucleus of NGC 454 E, observed spectroscopically by Johansson (1988), revealed several emission lines and matched two of the empirical criteria proposed by Shuder & Osterbrock (1981) for a Seyfert galaxy: the line-width of Hα is larger than 300 km s^{-1} and the [OIII]λ5007Å/Hβ ratio is larger than 3. However, none of the high-excitation lines expected in this case, as HeII, were detected (see also Donzelli & Pastoriza 2000; Tanvuia et al. 2003). The AGN type of the nucleus has been recently detailed by Marchese et al. (2012). Their analysis of *SWIFT*, XMM-*Netwon* and *Suzaku* observations characterizes the NGC454 E nucleus as a "changing look" AGN. This is a class of AGN showing significant variation of the absorbing column density along the line of sight.

The West region of the pair labeled in Figure 1 as W (NGC 454 W hereafter) has been considered by Johansson (1988) as the debris of an irregular galaxy. However, the galaxy is so widely distorted by the on-going interaction that the classification is difficult. Stiavelli et al. (1998) suggested that it is the debris of a disk galaxy. NGC 454 W is a starburst galaxy, as shown by the Hα image of Johansson (1988, their Figure 6a and 6b). The spectrum of NGC 454 W shows emission lines whose ratios, according to the above authors, are due to photo-ionization by star formation and shock heating.

The NGC 454 E region is particularly distorted in the North-West side. This region, label as T (NGC 454 T hereafter) in Figure 1, has been studied by Stiavelli et al. (1998) which found this is composed by a mix of the stellar populations of the NGC 454 E and the NGC 454 W. Moreover, they found a similarity between the color of NGC 454 T region and that of the nearby sky and speculated about the presence of a faint tail of stripped material in this region not detected by the HST observations.

The picture of the NGC 454 system is completed by three blue knots, NGC 454 SW, NGC 454 SE and NGC 454 S, well detached from NGC 454 E, and likely connected to NGC 454 W (Johansson 1988; Stiavelli et al. 1998). Johansson (1988) suggested that these are newly formed globular clusters of 3×10^6 $M_\odot$ and 1-5$\times10^7$ years stellar age. Recently several investigations suggest that young independent stellar systems at $z \simeq 0$ start to form in tidal debris (see e.g. review by Lelli et al. 2015).

Table 1 summarizes some basic characteristics of NGC 454 E and W which appear as a prototype of an encounter/merger (ΔV_{hel}=1$\pm$2 km s^{-1} Tanvuia et al. (2003)) between a late and an early-type galaxy, this latter having an active and peculiar Seyfert-like nucleus. Therefore, the study of this system can make progresses in our understanding of the effects of a wet interaction.

Our contribution consists of two correlated pieces of ob-

Table 1. NGC 454 system basic properties from the literature

NGC 454 E		Ref.
Morphology	E/S0 pec	(1,2)
R.A. (2000)	$1^h\ 14^m\ 25.2^s$	(3)
Decl. (2000)	-55° 23' 47"	(3)
V_{hel}	3635±2 km s^{-1}	(3)
$(B-V)_0$	0.80	(1)
$(U-B)_0$	0.31	(1)
L_X (0.1-0.3 keV) XMM	2.8 10^{39} erg cm^{-2} s^{-1}	(4)
L_X (0.1-0.3 keV) Suzaku	5.6 10^{39} erg cm^{-2} s^{-1}	(4)
L_X (0.1-0.3 keV) XMM	2.5 10^{42} erg cm^{-2} s^{-1}	(5)
L_X (0.1-0.3 keV) Suzaku	7.2 10^{42} erg cm^{-2} s^{-1}	(5)
L_X (14-150 keV) XMM	4.8 10^{42} erg cm^{-2} s^{-1}	(5)
L_X (14-150 keV) Suzaku	1.4 10^{42} erg cm^{-2} s^{-1}	(5)
NGC 454 W		
Morphology	Irr, (disrupted) Sp	(1,2)
R.A. (2000)	$1^h\ 14^m\ 20.1^s$	(3)
Decl. (2000)	-55° 24' 02"	(3)
V_{hel}	3626±2 km s^{-1}	(3)
$(B-V)$	0.32	(1)
$(U-B)_0$	-0.22	(1)
M(H_2) [10^8 $M_\odot$]	< 2	(6)
V_{hel} adopted [km s^{-1}	3645	(7)
Distance [Mpc]	48.5±3.4	(7)
scale [kpc arcsec^{-1}]	0.235	(7)

References: (1) Johansson (1988) provides the mean corrected radial velocity; the morphology is uncertain (2) Stiavelli et al. (1998); (3) the Heliocentric velocities of the E and W components are derived from Tanvuia et al. (2003) and are consistent with the systemic velocity V_{hel}=3645 provided by NED we adopted; (4) Braito Valentina private communication; (5) Marchese et al. (2012) (6) Horellou & Booth (1997); (7) The adopted heliocentric velocity and the distance (Galactocentric GSR) of the NGC 454 system are from NED.

servational information: (1) the investigation of the multi-wavelength structure of NGC 454 E via the optical and UV surface photometry and (2) the analysis of the kinematics of the ionized gas component. The *Galaxy Evolution Explorer* (Morrissay et al. 2007, *GALEX)* showed the strength of UV observations in revealing rejuvenation episodes in otherwise old stellar systems (see e.g. Rampazzo et al. 2007; Marino et al. 2011; Rampazzo et al. 2011, and references therein). In this context, we investigate the Near UV (NUV hereafter) stellar structure of the NGC 454 system using *Swift* UVOT UV images (see also Rampazzo et al. 2017, and references therein). In order to study the ionized gas, connected to the ongoing star formation, we use the SOAR Adaptive Module (SAM) coupled with a Fabry-Perot to investigate its distribution, the 2D velocity and velocity dispersion fields of the Hα emission in NGC 454 W and in NGC 454 SW and SE stellar complexes, likely debris of NGC 454 W. We finally attempt to derive the parameters and the merger history of the system using simulations.

The paper is organized as follows. In Section 2 we present *SWIFT*-UVOT (§ 2.1) and the SAM+Fabry-Perot (§ 2.2) observations of NGC 454 and the reduction techniques used. The *Swift*-UVOT surface brightness photometry is presented in § 3. The ionized gas kinematics is presented in

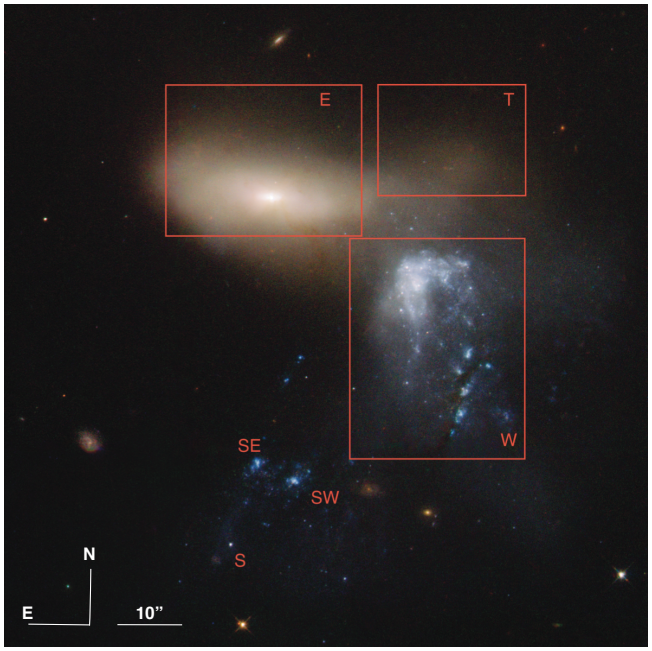

Figure 1. Color composite image of the NGC 454 system obtained with HST-Wide Field Planetary Camera 2 in the F450W (B), F606W (V), and F814W (I) filter by Stiavelli et al. (1998). The figure highlights the different regions of the system following Johansson (1988) E and W areas include the early-type and the late-type member of the pair, respectively; S, SW and SE are knots likely connected to the W member. T is an area introduced by Stiavelli et al. (1998) (see text). The size of the FOV is 1.66′.

§ 4, the diagnostic digrams of H II complexes are discussed in § 5, while § 6 considers the Hα line profile decomposition. In § 7 our results are discussed in the context of galaxy-galaxy interaction and compared with Smoothed Particle Hydrodynamic (SPH) simulation with chemo-photometric implementation in § 7.2. Finally in § 8, we give the summary and draw general conclusion.

2 OBSERVATION AND DATA REDUCTION

2.1 SWIFT-UVOT observations

UVOT is a 30 cm telescope in the *SWIFT* platform operating both in imaging and spectroscopy modes (Roming et al. 2005). We mined the UVOT archive in the ASDC-ASI Science Data Center retrieving the 00035244003 product including images of the NGC 454 system in all six filters available. Table 3 gives the characteristics of these filters and calibrations are discussed in Breeveld et al. (2010, 2011).

The archival UVOT un-binned images have a scale of 0.″5/pixel. Images were processed using the procedure described in http://www.swift.ac.uk/analysis/uvot/. All the images taken in the same filter are combined in a single image using UVOTSUM to improve the S/N and to enhance the visibility of NUV features of low surface brightness. The final data set of the $UVW2$, $UVM2$, $UVW1$, U, B, V images have total exposure times reported in Table 3.

UVOT is a photon counting instrument and, as such, is subject to coincidence loss when the throughput is high,

whether due to background or source counts, which may result in an undercounting of the flux affecting the brightness of the source. Count rates less than 0.01 counts s^{-1} $pixel^{-1}$ are affected by at most 1% and count rate less than 0.1 counts s^{-1} $pixel^{-1}$ by at most 12% due to coincidence loss (Breeveld et al. 2011, their Figure 6).

Coincidence loss effects can be corrected in the case of point sources (Poole et al. 2008; Breeveld et al. 2010). For extended sources a correction process has been performed for NGC 4449, a Magellanic-type irregular galaxy with bright star forming regions, by Karczewski et al. (2013). Even though their whole field is affected, the authors calculate that the statistical and systematic uncertainties in their total fluxes amount to ≈ 7-9% overall, for the NUV and the optical bands.

We checked, indeed, that in UV filters the coincidence losses may involve only few central pixels of the Irr galaxy, i.e., NGC 454 W, never exceeding 0.1 count s^{-1} px^{-1} (in particular, the maximum value of the count rates is 0.043, 0.028, and 0.047 count s^{-1} px^{-1} in $UVW2$, $UVM2$ and $UVW1$ filters respectively). Our NUV images are very slightly affected so we decided do not account for this effect. Optical images are more affected. In the NGC 454 W region the effect remains $\leq$ 0.1 count s^{-1} px^{-1} in all the bands, in particular it reaches 0.09, , 0.08, and 0.096 count s^{-1} px^{-1} in the U, B and V filters respectively. As far as NGC 454 E is concerned, in the U filter count rates are at most 0.084 count s^{-1} px^{-1}, and reach 0.2 in the B and V bands in the inner 5″. So, we add to the photometric error in Table 3 a further error of 12% in optical bands to account for this effect.

We compared our total magnitudes in Table 3 with Prugniel & Héraudeau (1998) which reported a total magnitude B=13.32±0.05 and 13.44±0.064, respectively for the whole NGC 454 system and for NGC 454 W. Once our measures are scaled to the Vega system (B=B[AB]+0.139) we have B=13.43±0.15 and B=13.65±0.12, in very good agreement with previous estimates.

Our $(B-V)$ color, integrated within a 31″ aperture and corrected for galactic absorption for NGC 454 E and NGC 454 W is 0.88±0.11 and 0.48±0.06, respectively, to be compared with 0.80 and 0.32 from Johansson (1988).

2.2 Fabry-Perot observation

Fabry-Perot (FP hereafter) observations[1] have been carried out on Sept 30th 2016 as part of the SAM-FP Early Science run at SOAR 4.1m telescope at Cerro Pachon (Chile). SAM-FP is a new instrument, available at SOAR, combining the adaptative optics SAM (Tokovinin et al. 2010a,b) and a scanning Queensgate ET70 Etalon (Mendes de Oliveira et al. 2017). The SAM module has been conceived to deliver a 0.″35 angular resolution across a 3′×3′ FoV, depending on atmospheric condition, using Ground Layer Adaptive Optics (GLAO). The SAM instrument detector is a 4K×4K CCD with a scale image scale of 0.″0454 (physical pixel of 15μ) on the sky (Fraga et al. 2013). The present observations have been binned over 4×4 pixels resulting in a scale of 0.″18/px. The interferometer used is a ET70 Queensgate scanning FP with an order of p=609@Hα. The FP piezos are driven by a CS100 controller, positioned at the telescope. Table 2 gives the journal of observation with the characteristic of the etalon we used. At the center of the Free Spectral Range we adopt the systemic velocity of 3645 km s^{-1} provided by `NED` (see also Donzelli & Pastoriza 2000; Tanvuia et al. 2003, as more recent and independent sources).

Data have been reduced using home made Python macros to handle Multi Extension Files from SAM and building the data cube, some `IRAF`[2] specific tasks and `Adhocw` [3] software procedures have been used to handle the cube. The data reduction procedure has been extensively described by Amram et al. (1996) and Epinat et al. (2008). The first step, before the phase correction, is to perform the standard CCD data reduction by applying bias and flat-field corrections under `IRAF` as well as the cosmic removal using `L.A.cosmic` procedure (van Dokkum 2001). Linear combinations of dark images have been used to removed CCD patterns in different frames.

In addition to these canonical operations, it is necessary to check and correct for several effects, such as, misalignment of data cube frames (due to bad guiding), sky transparency variation throughout the cube, and seeing variation. Misalignment variation across the 43 frames of the data cube is less than half pixel, thus it is negligible. The sky transparency has been corrected using a star in the FoV. It varies between 81% to 98% during the observation: each frame has been corrected accordingly using one channel as a reference. The same star is also used to map the corrected seeing variation ranging from 0.″71 to 0.″90. We then applied a 2D spatial Gaussian smoothing equivalent to the worse estimated corrected seeing (0.″90). Phase map and phase correction have been performed using the `Adhocw` package and by scanning of the narrow Ne 6599Å line under the same observing conditions. The velocities measured are very accurate compared to the systemic velocity in Table 1, with an error of a fraction of a channel width (i.e., $<$ 3 km s^{-1}) over the whole FoV. The signal measured along the scanning sequence was separated into two parts: (i) an almost constant level produced by the continuum light in a 15Å passband around Hα (continuum map, not presented in this work); (ii) a varying part produced by the Hα line (Hα integrated flux map). The continuum is computed by taking the mean signal outside the emission line. The Hα integrated flux map was obtained by integrating the monochromatic profile in each pixel. The velocity sampling was 11.6 km s^{-1}. Strong OH night-sky lines passing through the filters were subtracted by determining the level of emission away from our target (Laval et al. 1987).

The velocity dispersion (σ hereafter) is derived from the determination of the FWHM from the determined profile. Then the real dispersion velocity is found supposing that different contributions follow a gaussian function.

$$\sigma^2_{real} = \sigma^2_{obs} - \sigma^2_{th} - \sigma^2_{inst}$$

[1] All Fabry-Perot data (cubes and moment maps) are available at cesam.lam.fr/fabryperot/

[2] `IRAF` is distributed by the National Optical Astronomy Observatories, which are operated by the Association of Universities for Research in Astronomy, Inc., under cooperative agreement with the National Science Foundation.

[3] Available at: https://cesam.lam.fr/fabryperot/index/softwares

Table 2. Instrumental setup

Fabry-Perot Parameters	Values
Telescope	SOAR 4.1m
Date	Sept. 30^{th}2016
Instrument	SAM-FP [a]
Detector	CCD
Pixel size (binned)	0.″18/px (0.″0454×4)
Calibration neon light (λ)	6598.95 Å
Resolution ($\lambda/\Delta\lambda$)	10700
Filter Characteristics	
Filter Central wavelength	6642Å
Filter Transmission	80%@6642Å
Filter FWHM ($\Delta\lambda$)	15Å
Interferometer Characteristics	
Interferometer order at Hα	609
Free spectral range at Hα (km s^{-1})	498
Number of scanning steps	43
Sampling steps	0.26 Å (11.60 km s^{-1})
Total Exposure Time	1.1h (90s/channel)

[a] Tokovinin et al. (2010a,b)

where σ_{inst} = 12.82 km s^{-1} is the instrument broadening deduced from the Ne calibration lamp and σ_{th} = 9.1 km s^{-1} is the thermal broadening of the Hα line.

3 SURFACE PHOTOMETRY FROM *SWIFT*-UVOT OBSERVATIONS

The color composite images in optical and NUV bands from the *Swift*-UVOT observations are shown in the top panels of Figure 2. Images show that the NGC 454 W emission dominates in the NUV bands. In NUV NGC 454 W1- W6 complexes appear included in a unique envelope which elongates up to NGC 454 SW and SE. In NUV two complexes, already revealed in Hα by Johansson (1988), are projected between NGC 454 SE and NGC 454 W. NGC 454 S, shown in Figure 1, appears connected to NGC 454 SW.

We derived the luminosity profiles and $(UVM2 - V)$ and $(B - V)$ color profiles of NGC 454 E. They are shown in the middle and bottom panels of Figure 2. Luminosity profiles have been derived using the task ELLIPSE in the package IRAF (Jedrzejewski 1987). These are not corrected for galactic extinction. Since we aim at parameterizing the galaxy structure we have truncated the profile at ≈35″ ($a^{1/4}$ = 2.43) where the distortion by NGC 454 W, in particular in NUV, becomes dominant.

The $(B-V)$ color profile tends to become bluer with the galacto-centric distance as shown in Stiavelli et al. (1998). The trend is much clear along the $(UVM2-V)$ color profile.

Stiavelli et al. (1998) parametrized the HST luminosty profiles with a composite bulge plus disk model. Due to our poorer resolution and PSF, to parametrize the trend of optical and NUV surface brightness profiles we adopt a Sérsic $r^{1/n}$ law (Sersic 1968), widely used for early-type galaxies as a generalization of the $r^{1/4}$ de Vaucouleurs (1948) law (see e.g. Rampazzo et al. 2017, and references therein). We best fit a Sérsic law convolved with a PSF, using a custom IDL routine based on the MPFit package (Markwardt et al. 2009), accounting for errors in the surface photometry. The PSF model is a Gaussian of given FWHM and the convolution is computed using FFT on oversampled vectors. We use the nominal value of the FWHM of the PSF of the UVOT filters. The residuals, $\mu - \mu_{Sersic}$, are shown in two panels of Figures 3, together with the values of the Sérsic indices for each of the UVOT bands reported in the top right corner of the two panels. The Sérsic indices are in the range 1.09±0.13≤ n ≤1.79±0.06

We remind that the Sérsic law has three special cases when n=1, the value for an exponential profile, and $n = 0.5$, for a Gaussian luminosity profile and n=4 for a bulge. The range of our Sérsic indices suggests that NGC 454 E has a disk. Residuals in Figure 3 shows a trend starting at about $a^{1/4} \simeq 1.6''$ consistently with a clear change in color in the $(UVM2 - V)$ color profile.

4 IONIZED GAS MOMENT MAPS

We extract from SAM+FP observations the monochromatic Hα emission map, the radial velocity and velocity dispersion maps. In Figure 4 we show HST F450W image (Stiavelli et al. 1998) (top left panel) on the same scale with our Hα monochromatic map (bottom left panel), heliocentric radial velocity map (top right panel), and velocity dispersion map (bottom right panel) of the system, corrected from broadening.

4.1 Hα monochromatic intensity map

Both narrow band imaging (Johansson 1988) and spectroscopy (Donzelli & Pastoriza 2000; Tanvuia et al. 2003) revealed Hα emission in the NGC 454 system. The bottom left panel of Figure 4 shows the Hα monochromatic intensity (I) map detected by our FP observations. Hα emission is revealed in the nucleus of NGC 454 E, in the NGC 454 W region and in the NGC 454 SE and SW complexes. NGC 454 W region shows a structured Hα emission. In this region we spot 6 complexes we labeled from W1 to W6, roughly from North to South, as shown in Figure 4 (bottom left panel).

NGC454 E has a Seyfert 2-type nucleus with broad, 250 and 300 km s^{-1}, emission line profiles (Johansson 1988). That fits into the Free Spectral Range of our etalon (almost 500 km s^{-1}). We apply a 5×5 px (0.212×0.212 kpc) boxcar smoothing to enhance the signal in the nuclear zone. The emission extends 3.″3 × 2.″0 (0.8 kpc × 0.7 kpc) around the center of NGC 454 E. Integrating the signal within boxes (see Figure 5) along the line connecting the NGC 454 E nucleus to the brightest complex of NGC 454 W (we labeled W1) we reveal emission lines whose profiles have complex shapes.

The W1 complex is the brightest in NGC 454 W, showing a nearly circular shape and a diameter of 5.″7 (1.3 kpc); the W6 complex is the larger, extending to 8.″5 (2 kpc). In the NUV map we may distinguish all the W1–W6 complexes but they appear more extended and interconnected than shown by our FP observations.

The NGC 454 SW and NGC 454 SE emission complexes shown in Figure 4 are relatively weaker than the W1–W6 complexes. We need to integrate the signal within 5×5 pixels bins to detect a connection between these complexes as

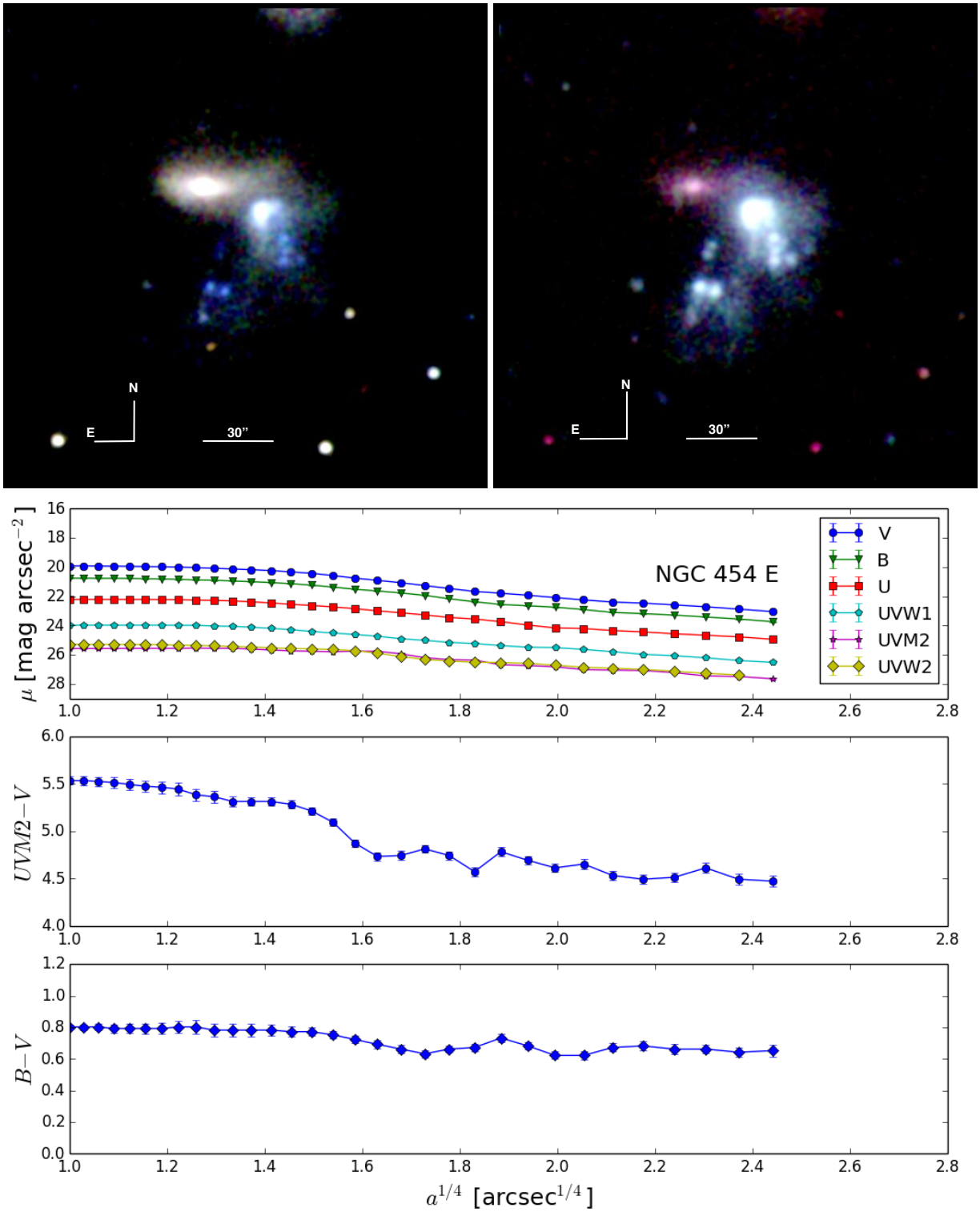

Figure 2. (top panels) Optical image (*U blue*, *B green*, *V red*), on the left and UV color composite image (*UVW2 blue*, *UVM2 green*, *UVW1 red*), on the right, of the NGC 454 system as observed by *Swift*-UVOT. The images have been smoothed 2 × 2 pixels (resulting 1″×1″resolution). The total Field of View is 4′×4′. (middle panel) Luminosity profiles of NGC 454 E in the optical and NUV bands. Profiles are not corrected for coincidence loss and galactic absorption. (bottom panels) $(M2 - V)$ and $(B - V)$ color profiles in [AB] magnitudes corrected for galactic absorption.

Table 3. *Swift*-UVOT integrated magnitudes

Filter	$UVW2$	$UVM2$	$UVW1$	U	B	V
Central λ	2030[Å]	2231[Å]	2634[Å]	3501[Å]	4329[Å]	5402 [Å]
PSF (FWHM)	2″.92	2″.45	2″.37	2″.37	2″.19	2″.18
Zero Point [a]	19.11±0.03	18.54±0.03	18.95±0.03	19.36±0.02	18.98±0.02	17.88±0.01
Total exp. time	1325 [s]	2255 [s]	3040 [s]	652 [s]	453 [s]	762[s]
Integrated magnitudes	[AB mag]	[AB mag]	[AB mag]	[AB mag]	[AB mag]	[AB mag]
NGC 454 E	17.96±0.13	17.83±0.25	16.61±0.28	15.15±0.14	13.77±0.18	13.20±0.18
NGC 454 W	15.32±0.15	15.16±0.13	14.90±0.09	14.46±0.12	13.51±0.20	13.13±0.28

[a] provided by Breeveld et al. (2011) for converting UVOT count rates to AB mag. (Oke 1974).

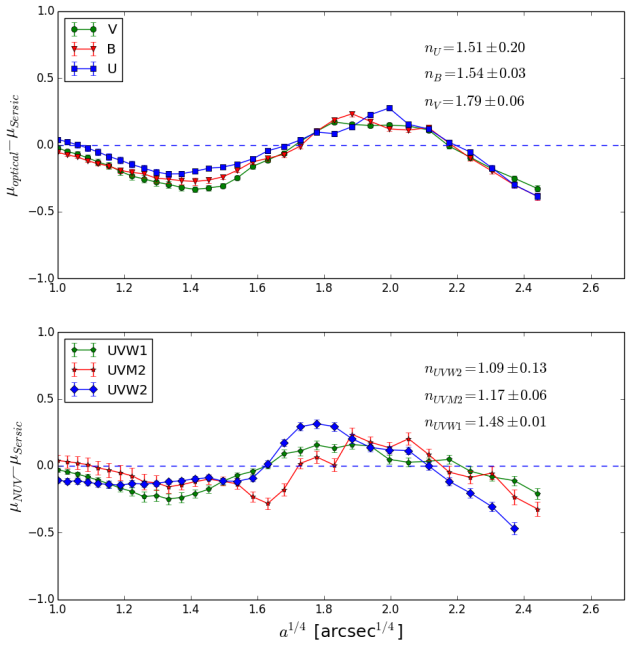

Figure 3. Residual from the fit of a single Sérsic $r^{1/n}$ law of the optical (top panel) and NUV (bottom panel) luminosity profiles. The value of the Sérsic indices, for each UVOT band are reported on the top right side of the figure. The values of the indices suggest the presence of a disk structure.

shown in the Johansson's Hα narrow band image. The bottom panels of Figure 6 show emission lines profiles in several areas of NGC 454 W, NGC 454 SE and NGC 454 SW.

Both the Hα image by Johansson (1988) and in our NUV images show an elongated emission region between NGC 454 SW and NGC 454 W1 complex, weaker than the other regions. We also detect emission in between the SW, SE complex and the SW1 region (see Figure 4). Our observation is showing a much smaller extension (1″.1 corresponding to 0.3 kpc) compared to Johansson (1988).

To summarize, the W1–W6 as well as SW and SE in NGC 454 W are huge (up to 2 kpc wide) complexes of ionized interstellar medium (ISM hereafter). Ionized ISM is also found in NGC 454 E center and along the line connecting it to NGC 454 W1 complex.

4.2 Radial velocity map

Figure 4 (top right panel) shows the 2D radial velocity, V_r, map of NGC 454. NGC 454 E velocity field is difficult to interpret because this object is an AGN showing large line profiles, almost covering our free spectral range. Nevertheless, a velocity gradient of 130 km s^{-1}, across 4″(0.94 kpc), is measured.

Velocities in the NGC 454 W range over 70 km s^{-1}, from maximum of 3645 km s^{-1} measured in the W2 complex to a minimum of 3575 km s^{-1} in the southern tip of W6 complex. None of the W1–W6 complexes has a rotation pattern. The W6 complex shows a velocity gradient of 35 km s^{-1} across a length of 8″.3 (1.95 kpc). The NGC 454 SW and NGC 454 SE complexes do not present velocity gradients. With respect to the W1-W6 complexes the SW and SE complexes are receding with a systemic velocity of 3725 km s^{-1} and 3691 km s^{-1}, respectively, with a velocity difference ΔV ≃115-145 km s^{-1} with respect to W1 complex.

4.3 Velocity dispersion map

The velocity dispersion, σ, map is shown in the bottom right panel of Figure 4. As mentioned before, NGC 454 E shows very broad profiles, very close to our free spectral range. In those conditions, we prefer not to show a velocity dispersion map for this galaxy. We measure σ values ranging from 14 to 42 km s^{-1} in the W3, W4, W5, W6 complexes. σ values of NGC 454 SW and NGC 454 SE are homogeneous, between 20 and 29 km s^{-1} . We point out that values exceeding 10 - 20 km s^{-1} indicate supersonic motions (see e.g. Smith & Weedman 1970). The W1 complex shows the highest values, up to 66 km s^{-1}, while in the W2 complex, σ ranges from 13 to 32 km s^{-1}.

4.4 Emission between H II regions

Figure 5 and Figures 6 show several regions in between NGC 454 E and NGC 454 W1 (Figure 5), NGC 454 SW and NGC 454 SE (Figure 6 top) and between NGC 454 W3 W4 W5 and W6 (Figure 6 bottom).

Figure 5, regions 1 and 2 show the emission centered in the elliptical. As mentioned before, the center of NGC 454 E has a broad emission as shown in region 2. With an emission peak above 3800 (in relative units) and a background of 2500, region 2 has a very high intensity considering that

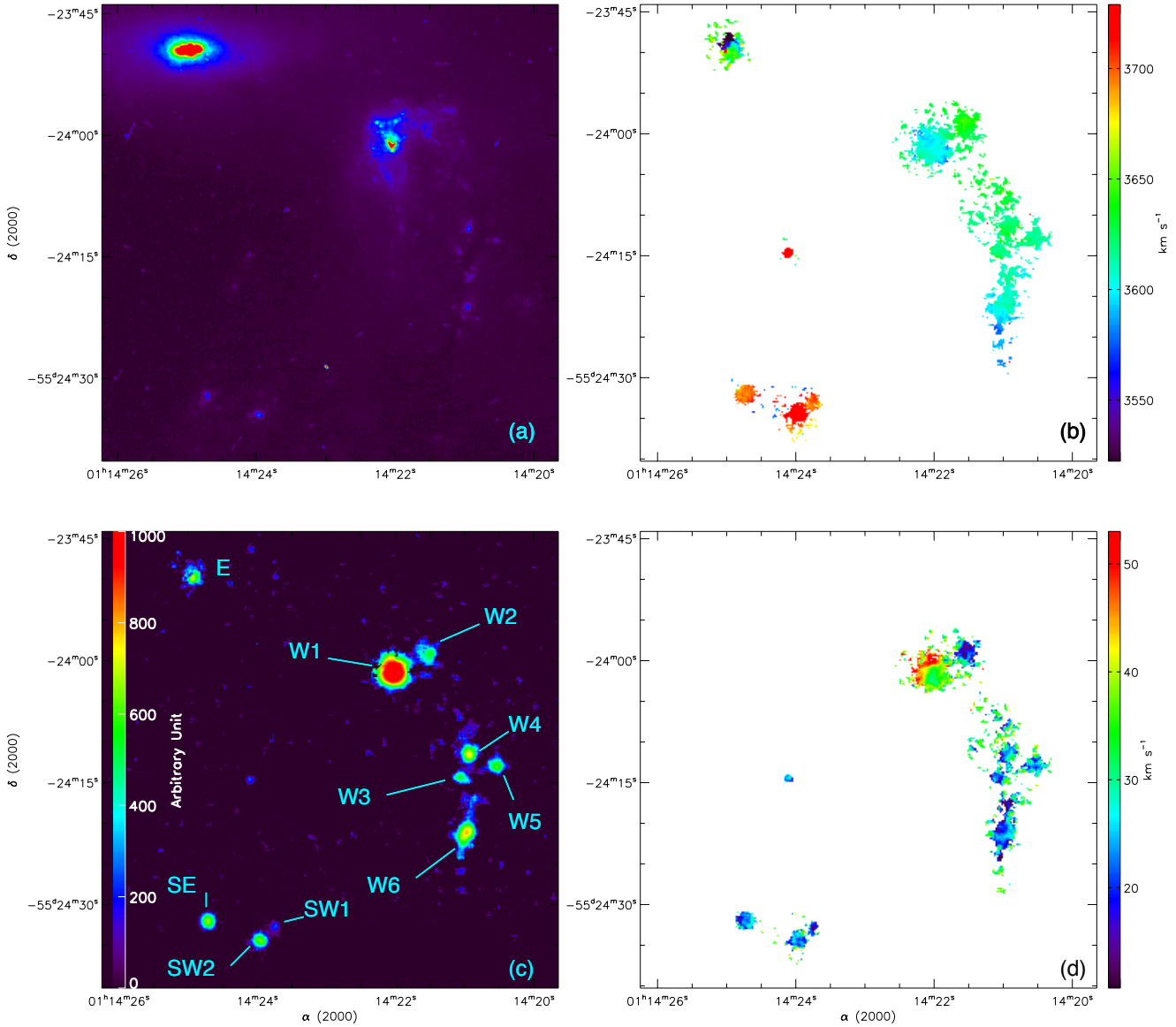

Figure 4. (a) HST F450W image of the NGC 454 system (Stiavelli et al. 1998), (b) 2D velocity field of Hα emission, centred on the NGC 454 systemic velocity, (c) monochromatic Hα map, and (d) Hα velocity dispersion map, corrected from broadening.

background is dominated by poisson noise and even if we consider that the profile has a FWHM of 300km s^{-1} (compared to the 500 km s^{-1} of the free spectral range), we still see the emission of the center of the elliptical. Regions 3 and 4 show areas in between NGC 454 E and NGC 454 W1, when region 3 shows a confortable emission line, region 4 shows the limit of our detection with an emission peak at one σ above the continuum level. Regions 5 and 6 show NGC 454 W1 emission, a detailed discussion about this latest is given in subsection 5.2 and section 6.

Figure 6 (top) shows emission profiles between the SE and SW regions. Emission is very clear across both regions. No substantial velocity gradient is visible even if the radial velocity of SW is 30 km s^{-1} lower than SE.

Figure 6 (bottom) shows the connection between the remaining regions (NGC 454 W3 to W6). Emission is strong and it is clear that all regions are connected. Zones 1 and 12 show asymmetric profiles, probably due to a second component. A radial velocity gradient is visible between the southern tip with zone 5 and region 1.

5 H II REGIONS DIAGNOSTIC DIAGRAMS

5.1 Description of the complexes

Complexes in NGC 454 W, share similar dynamical characteristics both with Giant H II Regions and the so-called H II Galaxies. Firstly, like GH IIRs, W1 has high supersonic profiles (Smith & Weedman 1970) and, secondly, the high velocity dispersion surrenders high monochromatic emission. Several studies using Fabry-Perot interferometer (Muñoz-Tuñón et al. 1996) found this signature in nearby

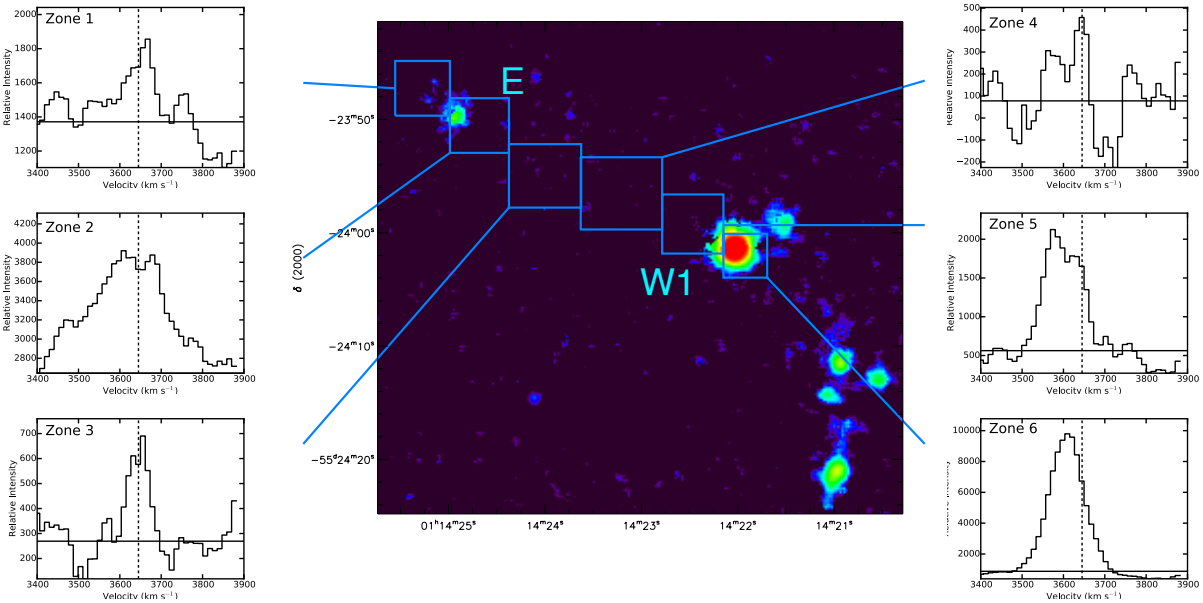

Figure 5. Emission profiles in the region NGC 454 E and NGC 454 W1. The vertical dotted line indicates the systemic velocity adopted V_{hel}=3645 km s^{-1}.The horizontal line indicates the mean continuum level. The map corresponds to the monochromatic emission.

Giant H II Region, like NGC 604. More recently, still using Fabry-Perot and IFU spectroscopy Bordalo et al. (2009); Moiseev & Lozinskaya (2012); Plana & Carvalho (2017), evidences have been found of such signature within dwarf H II galaxies.

Figure 7 considers three different diagnostic diagrams used to study the kinematics of H II regions These diagnostic diagrams are shown for NGC 454 W complexes (W1-W6 identified in Figure 4) and for NGC 454 SW and SE regions.

The W1 complex has the larger intensity range. We will discuss the $(I-\sigma)$ regimes in this region in Section 5.2 with a statistical approach.

The panels (a) in Figure 7 represent the intensity vs the dispersion velocity (sigma). The W2 – W6 as well as SW1, SW2 and SE complexes show similar intensity and sigma ranges. In W3 – W6 as well as NGC 454 SW and SE complexes the scatter of σ increases as the intensity decreases. As discussed by Moiseev & Lozinskaya (2012) (their Figure 6) this shape is produced within star forming complexes with significant excursion of gas densities, indicating low density, turbulent ISM. At high density (high intensity) regime H II regions have either nearly constant or low scatter σ. However, towards lower density (low intensity) the high perturbed/turbulent gas surrounding H II regions may emerge so decreasing the intensity the σ scatter may increase. We have separated the different regions: W3, W4, W5 and W6 as SE, SW1 and SW2 complexes in these diagrams. The last row of Figure 7 shows the SE, SW1 and SW2 complexes I vs σ diagram, but none of the three complexes shows a different pattern. Introduced by Muñoz-Tuñón et al. (1996), the $(I-\sigma)$ diagram has been used by those authors to identify expanding shells by localising inclined bands. This interpretation is based on the fact that the velocity dispersion should be higher at the center of the shell and the intensity lower because less material is crossed along the line of sight than at the shell inner and outer edges. Assuming this pattern, the inclination of the band can also be interpreted in term of age of the shell itself. As the shell ages, the velocity dispersion at the center decreases as well as the intensity difference between the center and inner edge of the shell (see figure 3 in Muñoz-Tuñón et al. 1996). The Moiseev & Lozinskaya (2012) interpretation tends to act for larger scales, where high velocity dispersion is not related to specific expanding shells, but rather belong to the diffuse low brightness emission.

The panels (b) in Figure 7 represent the intensity vs. radial velocity, $(I-V_r)$, diagram of W1-W6 complexes in NGC 454 W, and in the SW1, SW2 and SE.

The range of radial velocity, V_r, within complexes is small, of the order of 20-40 km s^{-1} in the W3 – W6 and NGC 454 SW1, SW2 and SE complexes. Large radial velocity excursion at all intensities is found in W2. The W3, W4, W5 and W6 complexes show different radial velocities, with W4 having the highest and W6 the lowest. W6 velocity range is larger because of the velocity gradient we already mentioned in Section 4. The separation in radial velocity between the SE, SW1 and SW2 complexes is shown in the plot (b) of the last row of Figure 7. The complex NGC 454 SE, SW and SW2 have a small variation, 10-20 km s^{-1}, of V_r while the monochromatic intensity range is similar to W3 – W6 complexes. It also appears that SW1 complex has a closer radial velocity with SE than with SW2. According to (Bordalo et al. 2009) (their figure 13b), a vertical band in this diagram, representing a velocity variation in a short intensity range, means a radial motion such as an expansion, but it could also means an inflow. The physical mechanisms in action are several including turbulence, winds, flows, bubbles or the self gravity of the complexes at different scales. Even if a vertical band can appear in the plot representing W2 (second row), it is difficult to interpret it as a signature of a radial motion, the intensity range being too wide.

The panels (c) in Figure 7 consider the $(V_r-\sigma)$ diagrams

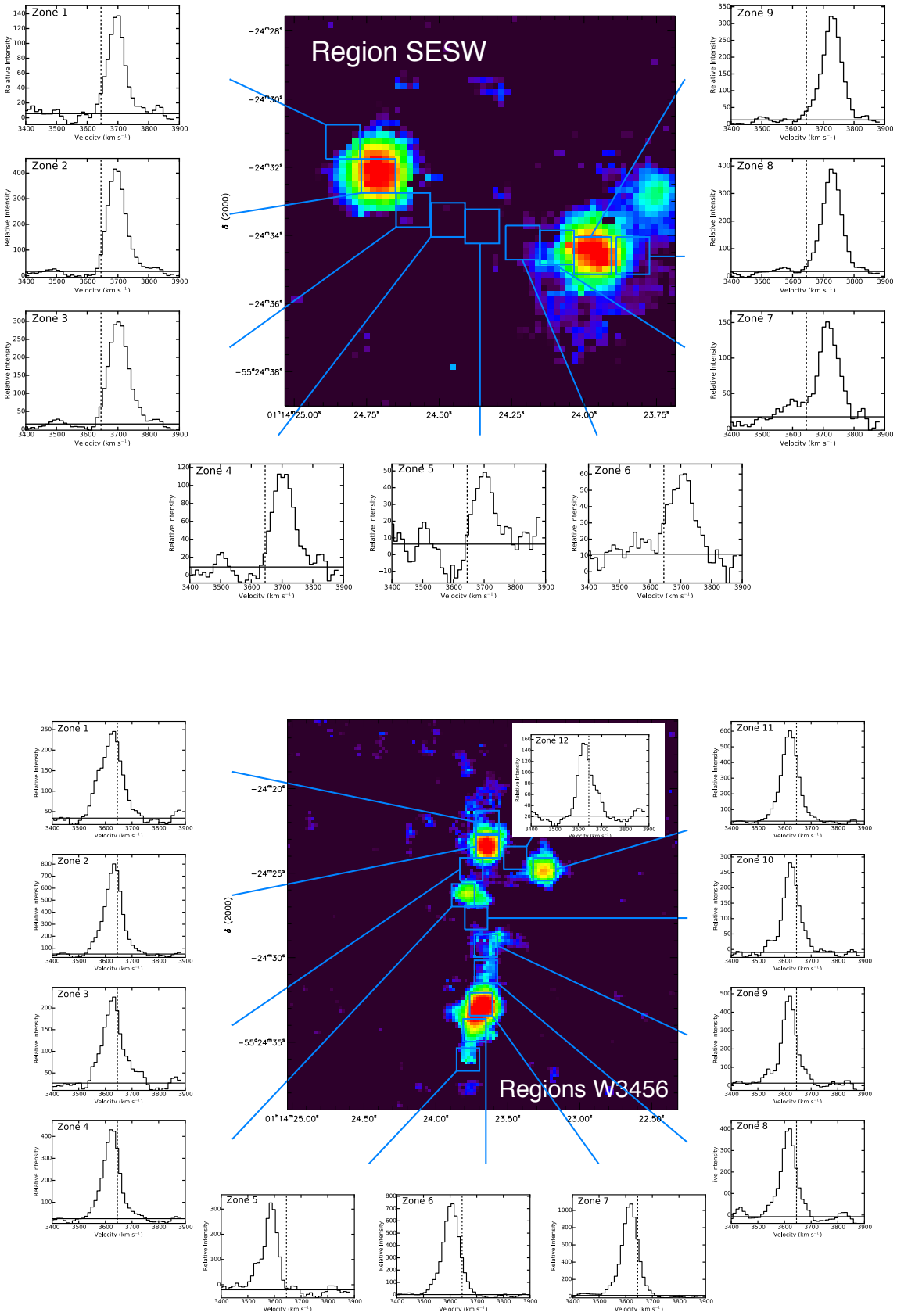

Figure 6. Emission profiles in NGC 454 SE and NGC 454 SW (top panel) and in the NGC 454 W region between W3 and W6 complexes (bottom panel). The vertical dotted line indicates the systemic velocity adopted V_{hel}=3645 km s^{-1}.The horizontal line indicates the mean continuum level. The map corresponds to the monochromatic emission.

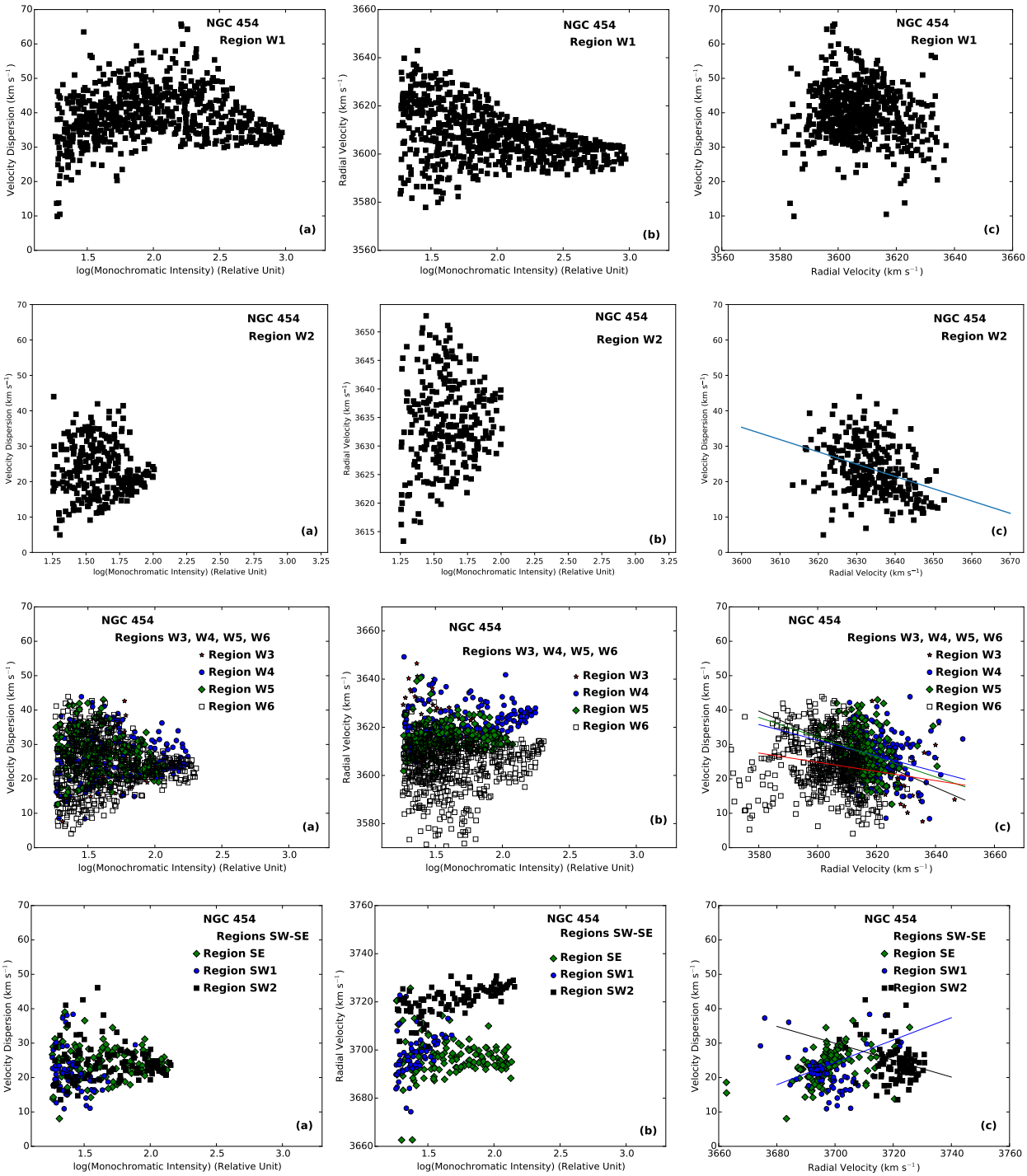

Figure 7. From top to bottom: panels plot (a) $(I-\sigma)$, panels (b) $(I-V_r)$, panels (c) $(V_{hel}-\sigma)$ diagnostic diagrams in W1-W6 complexes in NGC 454 W and in the NGC 454 SE and SW complexes. The plot results from a single Gaussian fit to the line profile. Solid lines in $V_r-\sigma$ diagrams represent the linear regressions applied when the Pearson's correlation test is robust.

in the same regions. Bordalo et al. (2009) pointed out that a dependence between the variables may indicate systematic relative motion of the clouds in the complex. They presented an idealized pattern for this diagram. Inclined $(V_r-\sigma)$ patterns would represent systematic motion like Champagne flows, such that cloud of gas with high σ moves away from us (positive slope) or toward us (negative slope).

We perform a standard Pearson's product-moment correlation test for the different complexes of NGC 454, in order to show the existence of systematic motions mentioned above. Except for W1 and SW1, all regions show weak-moderate correlation, according this test. W2 has a correlation coefficient of -0.34, W3 of -0.43, W4 of -0.23, W5 of -0.27, W6 of -0.17. The SE and SW2 regions also have a

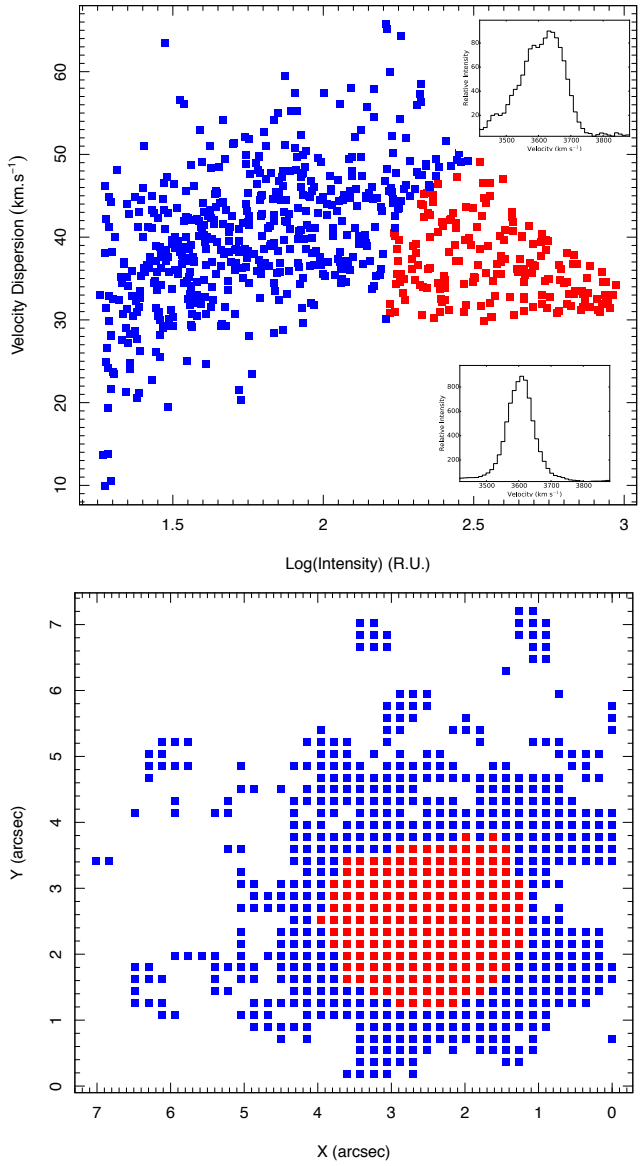

Figure 8. (bottom panel) The 3×3 pixels sampling of the NGC 454 W1 complex. (top panel) $(I-\sigma)$ plot. The colors highlight two regions, the central and outskirts, with different regimes (see Section 5.2 for details). Top profile shows a typical monochromatic emission representative of the blue points, and bottom profile representative of the red points.

weak-moderate correlation with a coefficient of 0.48 and -0.25. All of them with a 99.9% confidence level. The case of SW1 is a bit more complex. The Pearson test is not conclusive and we decide to use a robust correlation test in order to put lower weight in marginal points. Using the `WRS2` package in `R`, we found a correlation of -0.2 with a 90% confidence level.

We perform a simple linear regression (the solid line in Figure 7 panels (c)) for the regions where the Pearson test shows a weak-moderate correlation: W2 to W6, SE and SW2. In this context W2 and SW2 regions can be interpreted as complexes with relatively high dispersion, moving toward the observer (negative slope). In the case of the SE complex, the slope is positive and it can be interpreted as a complex moving away from the observer.

Previous studies, on Giant H II Region or emitting dwarf galaxies, also used those diagnostic diagrams when these objects are smaller and the scale resolution much smaller than here. For example NGC 604 study from Muñoz-Tuñón et al. (1996) or dwarf galaxies from Moiseev & Lozinskaya (2012) or Bordalo et al. (2009) have respectively scale resolution of 3.31pc/″and 21pc/″. This is ten times smaller than our object. Even though, we found remarkable similarities between diagnostics diagrams.

5.2 Statistical analysis of the $(I-\sigma)$ diagrams for W1 complex

We use the `R` statistical package (`R` Development Core Team 2009) to analyze the $(I-\sigma)$ diagram of the W1 complex. `R` is largely use in different statistical analysis. The `Mclust` routine only has been recently used in astrophysics by (Einasto et al. 2010) to detect structure in galaxies clusters. We aim at finding how many independent components are present (task `Mclust`), to locate them in the diagram and in the σ map (so-called geographic location). `Mclust` is a `R` function for model-based clustering, classification, and density estimation based on finite Gaussian mixture modeling. An integrated approach to finite mixture models is provided, with routines that combine model-based hierarchical clustering and several tools for model selection (see Fraley & Raferty 2007).

For a bivariate random sample $\mathbf{x}$ be a realization from a finite mixture of $m > 1$ distributions, it should follow

$$p(\mathbf{x}|\pi, \{\mu_k, \Sigma_k\}) = \sum_k \pi_k \phi(\mathbf{x}|\mu_k, \Sigma_k), \quad (1)$$

where ϕ is the multivariate normal density

$$\phi(\mathbf{x}|\mu, \Sigma) = (2\pi)^{-d/2}|\Sigma|^{-1/2} \exp\{-\frac{1}{2}(\mathbf{x}-\mu)'\Sigma^{-1}(\mathbf{x}-\mu)\}, \quad (2)$$

$\pi = \{\pi_1, ..., \pi_m\}$ are the mixing weights or probabilities (such that $\pi_k > 0$ and $\sum_k^m \pi_k = 1$), (μ_k, Σ_k) are the mean the covariance matrix of the component k, and d is the dimension of the data. A central question in finite mixture modeling is how many components should be included in the mixture. In the multivariate setting, the volume, shape, and orientation of the covariances define different models (or parametrization) with their different geometric characteristics. In `Mclust`, the number of mixing components and the best covariance parameterization are selected using the Bayesian Information Criterion (BIC). The task outputs μ_k, Σ_k and π_k for k running from 1 to m. `Mclust` also relates each element in the dataset to a particular component in the mixture. To gain some flexibility on this classification, we combine the central result of `Mclust`, the number of components m, with the result of another `R` task: the `mvnormalmixEM` function.

This task belongs to the `mixtools` package, which provides a set of functions for analyzing a variety of finite mixture models. The general methodology used in `mixtools` involves the representation of the mixture problem as a

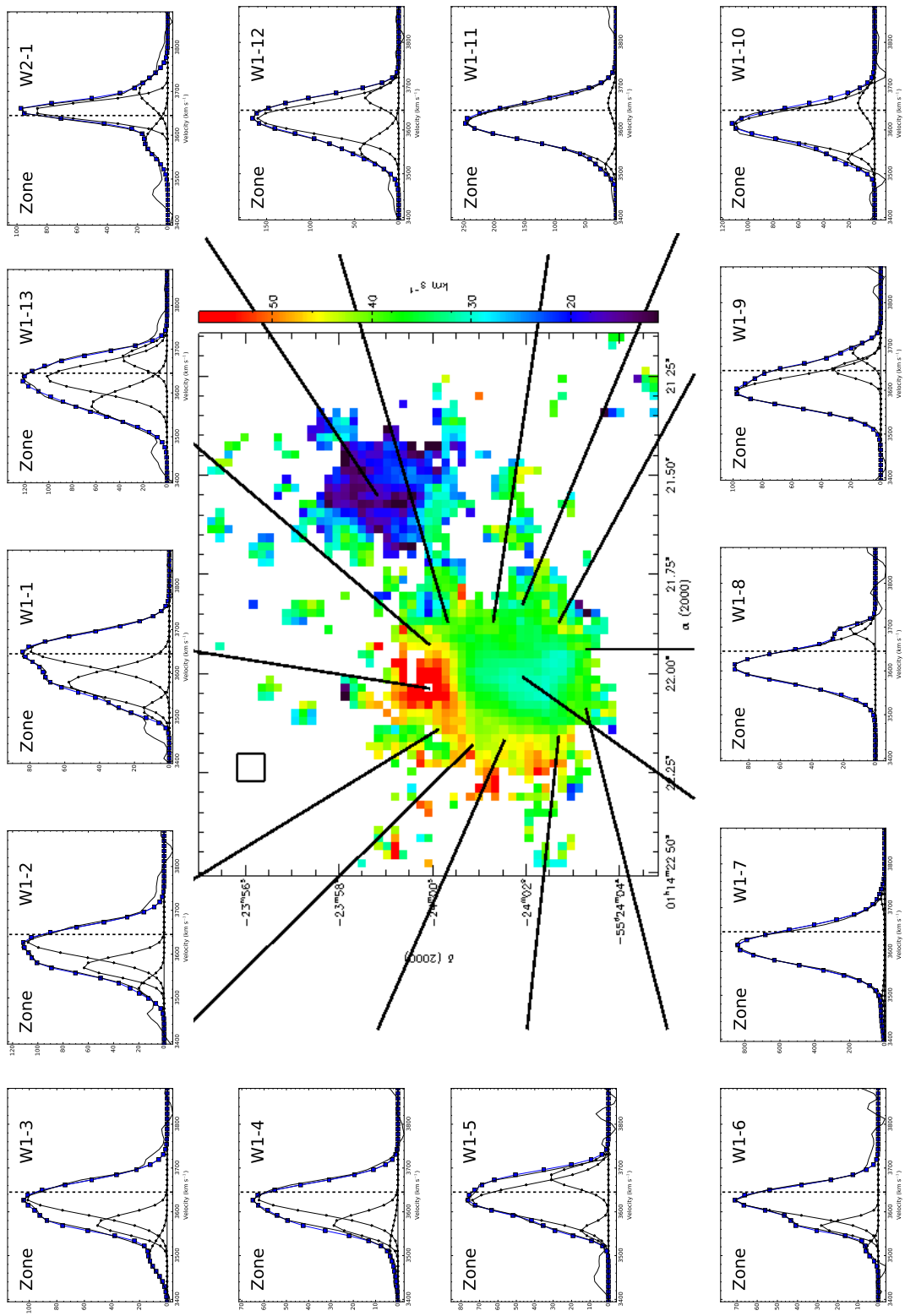

Figure 9. Integrated profiles in NGC 454 W1 and W2. Three Gaussian components fit of the emission lines in NGC 454 W1 and W2 complexes. Results of the fitting are reported in Table 3. The vertical dotted line indicates the systemic velocity adopted V_{hel}=3645 km s^{-1}.The horizontal line indicates the mean background level. The small square approximatively represents the size of the area of the integrated profiles (3 × 3px or 0.54″× 0.54″). The map corresponds to the dispersion velocity field, corrected from broadening.

Table 4. Hα line profiles Gaussian components in Region W1

Regions	Component 1			Component 2			Component 3		
	I	V_r	σ	I	V_r	σ	I	V_r	σ
	R.U.	[km s^{-1}]	[km s^{-1}]	R.U.	[km s^{-1}]	[km s^{-1}]	R.U.	[km s^{-1}]	[km s^{-1}]
(1)	(2)	(3)	(4)	(5)	(6)	(7)	(8)	(9)	(10)
Region W1 1	80.0	3654	22.2	58.0	3577	19.7	15.0	3516	11.3
Region W1 2	108.0	3629	20.7	64.0	3572	13.8	20.0	3522	13.8
Region W1 3	102.0	3632	22.2	51.0	3572	13.8	13.0	3499	21.2
Region W1 4	063.0	3632	20.7	29.0	3572	4.8	03.5	3522	27.1
Region W1 5	74.0	3624	22.2	32.0	3679	13.8	15.0	3557	09.9
Region W1 6	71.0	3627	18.7	28.5	3566	9.9	6.0	3514	10.1
Region W1 7	662.0	3611	24.6	25.0	3487	26.6	20.0	3725	22.1
Region W1 8	90.0	3609	22.6	16.5	3693	7.9	0.0	3383	00.0
Region W1 9	98.0	3596	21.2	33.0	3647	10.9	19.0	3687	12.9
Region W1 10	110.5	3610	21.2	21.0	3534	12.3	13.0	3661	16.8
Region W1 11	245.5	3617	24.6	18.0	3516	12.3	13.0	3661	16.8
Region W1 12	160.0	3627	20.7	44.0	3555	18.7	38.0	3673	12.4
Region W1 13	102.0	3635	19.7	64.0	3572	21.7	38.0	3680	13.8
Region W2 1	90.0	3656	12.3	19.0	3690	19.7	15.0	3586	20.7

The intensity, I, (col.s 2, 5 and 8) is in relative units (R.U.).

particular case of maximum likelihood estimation when the observations can be viewed as incomplete data. The code uses the Expectation-Maximization (EM) algorithm that maximizes the conditional expected log-likelihood at each M-step of the algorithm – see details in Benaglia et al. (2009). The code returns the posterior probabilities for each observation with respect to the m different components.

Since running `Mclust` results $m = 2$ components, we then use the task `mvnormalmixEM`, looking at two independent classes with 80% confidence in the $(I - \sigma)$ maps. Once these two classes have been found, we have represented them in the $(I - \sigma)$ diagram (Figure 8 upper panel) and in the σ map (Figure 8 lower panel). The figure clearly shows the two regions, one in the center (low dispersion and strong emission) and the other surrounding it (high dispersion and low emission). W1 is an extended ionized ISM complex so we cannot easily apply the interpretative scheme of H II regions. We may exclude that W1 may be interpreted as an expanding wind-blown bubble would have a different signature in a $(I - \sigma)$ map: σ values should decrease from the center to the edge of the shell, according Lagrois & Joncas (2009). The two regimes evidenced by the statistical approach support the picture proposed by Moiseev & Lozinskaya (2012) in which the W1 complex can be viewed as composed of a giant dense HII region in the central part and turbulent low-density gas cloud in its outskirt.

6 Hα LINE PROFILE DECOMPOSITION

Figure 4 (bottom right panel) shows the large range of σ in the W1 complex with respect to the other complexes in NGC 454 W as well as in the NGC 454 SW and SE. Figure 5 shows that emission lines are quite broad so that the high velocity dispersion in the W1 complex can be attributed to the presence of multiple components in the emission profiles. Figure 9 shows line profiles resulting from the mapping of the W1 and W2 complexes.

We perform a gaussian decomposition of the 14 Hα line profiles (13 in W1 and one in W2 as a sort of control field) shown in Figure 9. Each region represents a 3×3 pixels box ($0.54''\times0.54''$ area, 0.13×0.13 kpc). The decomposition has been performed using a home made program with three different Gaussian components. We first fit the brightest component, subtracts it and then fit the two others, until the final fit converges. Figure 9 shows the decomposition of these profiles and the location of areas in W1 and W2. Table 4 lists the characteristics of the three Gaussian components ordered by decreasing intensity component.

We are aware that a simple mathematical approach is always unsatisfactory, since the composition is not unique, but linked to a physical and kinematical interpretation, we are reasonably satisfied with the result.

Considering the results of the decomposition reported in Table 4, shown in Figure 9 we draw the following conclusions:

The central region, labeled W1 7, has a symmetrical profile when compared to all the others regions. The σ of the brightest Gaussian component of W1 complex has supersonic values between 20 and 25 $km\ s^{-1}$. The σ of the main component of all regions in W1 is larger than in W2.

With respect to the systemic velocity the main Gaussian component in W1 [1 to 5] is red-shifted while in the zones W1 [9 to 11] is blue-shifted, sketching a sort of rotation pattern being at the opposite sides of the W1 complex center. We also can note that positions of the second component with respect to the main one (second red-shifted component at one side of the W1 complex, and the second blue-shifted component at the other side) could be seen as a bipolar outflow due to massive star formation.

Several zones of W1 clearly show profiles with an apparent second component (e.g. W1 1, W1 2, W1 3, W1 4 and W1 6), while, in general, the other zones, including the W2 zone, need fainter components to fit the wings of the line profiles.

We conclude that even with multiple Gaussian fit analysis no un-ambiguous rotation pattern emerges in the W1

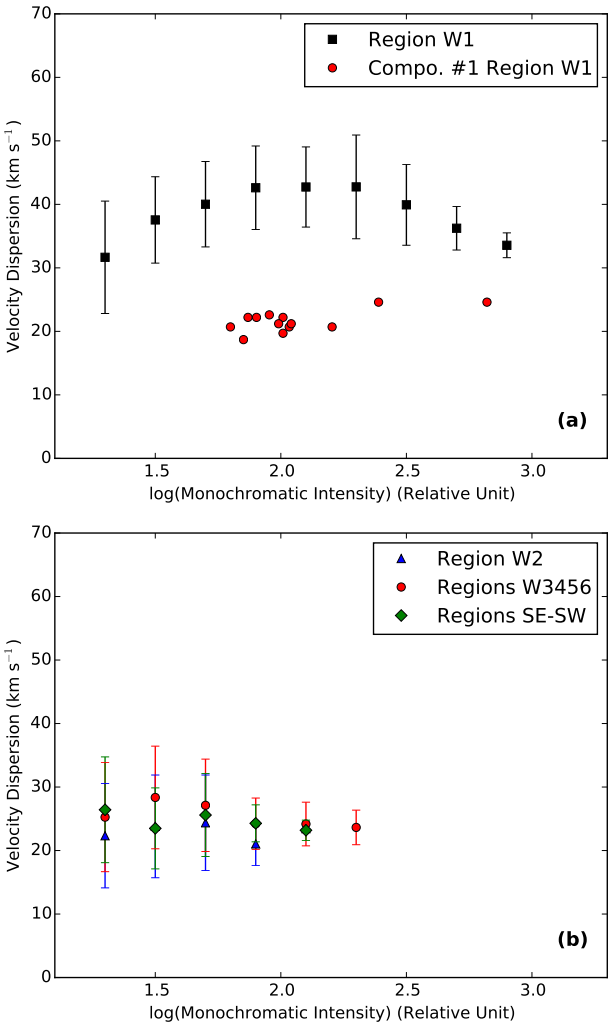

Figure 10. $(I-\sigma)$ diagnostic diagram for the W1 complex (top panel) and for the other complexes in NGC 454 W (bottom panel).The σ values are averaged over intensity bins. Red dots on W1 complex show the main component in line profile decomposition shown in Figure 9.

complex.

Using the characteristics of the Gaussian decomposition resumed in Table 4, we present, in Figure 10, a revised $(I-\sigma)$ diagnostic diagram, showing the $(I-\sigma)$ diagram for the main i.e. the brightest component. In Figure 10, top panel, we present the mean σ per intensity bin. The associated error bar represents the standard deviation in the bin. The red points represent the intensity and σ of the main component (see component 1 in Table 4). As mentioned before, σ is significantly lower, still largely supersonic and similar, on the average, to regions W2–W6, and SE-SW shown in the bottom panel of Figure 10. However, the σ of the main component in W1 shows a positive slope with I.

7 DISCUSSION

7.1 NGC 454: General view

In the NGC 454 system, there is no evidence of a velocity difference between the two members. The pair is furthermore strongly isolated as discussed in Appendix A. Our observations do not provide direct evidence of gas re-fueling of NGC 454 E on the part of NGC 454 W. We found, however, traces of ionized gas beyond the nucleus as shown in Figure 5. We detect broad emission line in the NGC 454 E nucleus but the small Free Spectral range prevents us to disentangle the presence of multiple components which may provide us information about possible gas infall (see e.g. Rampazzo et al. 2006; Font et al. 2011; Zaragoza-Cardiel et al. 2013, and references therein). However velocity gradient of about 130 km s^{-1} have been revealed in the central 4″. *Swift*-UVOT observations of NGC 454 E suggest that the galaxy is an S0 since a disk emerge in all the UVOT bands when a Sérsic law is fitted to the luminosity profile. Both the $(B-V)$ and $(M2-V)$ color profiles become bluer with the galactocentric distance supporting the presence of a disk (see also Rampazzo et al. 2017). The disk is itself strongly perturbed by the interaction as can deduced by the distortion in the NGC 454 T area (Figure 1).

Both Johansson (1988) and Stiavelli et al. (1998) speculated whether the morphology of NGC 454 W pair member was a spiral or an irregular galaxy, before the interaction. The galaxy, strongly star forming, dominates in the NUV images with respect to NGC 454 E. There is one evidence coming out from our velocity map: no rotation pattern are revealed, even in NGC 454 W1 complex. The velocity difference between the complexes reaches ≈140 km s^{-1} (Figure 4) if we include the NGC 454 SE an SW complexes, and it is about 60 km s^{-1} considering only NGC 454 W1-W6. To summarize, if NGC 454 W was a former spiral galaxy it appears completely distorted by the encounter and this latter is not at an early phase. In the next section, we will investigate the formation and evolution of this pair highligthening a possible interaction which matches the global properties of this pair, i.e. its total magnitude, morphology and multiwavelength SED.

NGC 454 SW, SE have a projected separation of ≈37.″19 (8.7 kpc) and ≈39.″86 (9.4 kpc) from the center of W1, i.e. they occupy a very peripheral position with respect to the bulk of the galaxy. Figure 1 and Figure 2 both show that there is a very faint connection with the rest of the galaxy. Our kinematical study suggests that the two complexes do not show a rotation pattern. So NGC 454 SW and SE differ from tidal dwarf candidates as described in Lelli et al. (2015). Figure 6 shows that Hα emission lines, detected also in between the SW and SE stellar complexes, are not composed of multiple components. According to the scheme proposed by Moiseev & Lozinskaya (2012) the $(I-\sigma)$ plots (Figure 7) suggests that the ionized gas in SW and SE stellar complexes have the characteristic of dense H II regions surrounded by low-density gas with considerable turbulent motions (see the scheme in their Figure 6) not dissimilar from W2-W6 complexes.

To summarize both the *Swift*-UVOT NUV observations and the diffuse Hα emission indicate that NGC 454 W, NGC 454 SW and SE complexes are strongly star forming regions. The anatomy of these complexes made using $(I-\sigma)$,

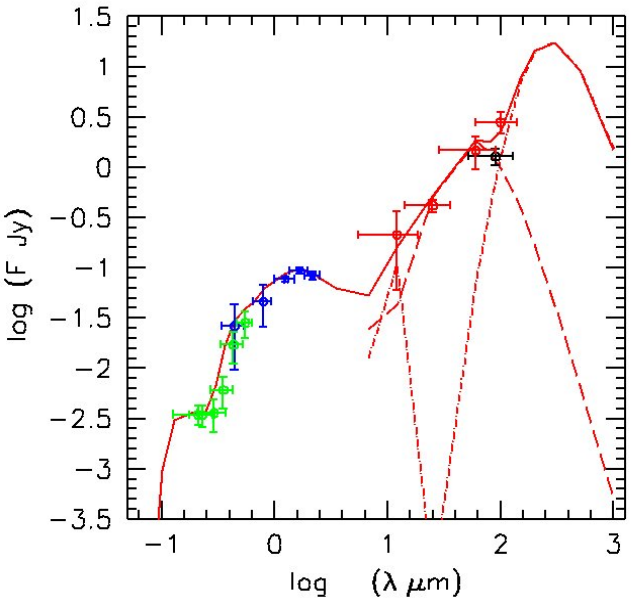

Figure 11. Observed spectral energy distribution(SED) of the whole NGC 454 system. The contribution of both the dust components to the FIR SED is also shown: dot-dashed and the long-dashed lines are the warm and the cold dust componenr, respectively (see text). The solid line represents the resulting SED. Green symbols represent our *Swift*-UVOT observations; blue symbols B, R, IRAS and 2MASS J, H, K measures. Red symbols are IRAS data while the black symbol is the AKARI/FIS detection.

$(I-V_r)$ and $(V_r-\sigma)$ diagnostic diagrams indicates that H II shells of different ages are present as well as zones of gas turbulence as expected by the interplay of star formation and SNae explosion in the IGM. Although our observations did not reveal direct evidence of gas infall on the center of NGC 454 E there is signatures of recent star formation, in addition to the non thermal Seyfert 2 emission. Mendoza-Castrejón et al. (2015) reported the presence in *Spitzer*-IRS spectra of polycyclic aromatic hydrocarbons (PAHs) which are connected to recent star formation episodes (see eg. Vega 2010; Rampazzo et al. 2013, and references therein).

7.2 Possible evolutionary scenario

We investigate the evolution of the NGC 454 system using smooth particle hydrodynamical (SPH) simulation with chemo-photometric implementation (Mazzei et al. 2014, and references therein). Simulations have been carried out with different total mass (for each system from 10^{13} $M_\odot$ to 10^{10} $M_\odot$), mass ratios (1:1 - 10:1), gas fraction (0.1 - 0.01) and particle number (initial total number from 40000 to 220000). All our simulations of galaxy formation and evolution start from collapsing triaxial systems (with triaxiality ratio, τ=0.84 (Mazzei et al. 2014), composed of dark matter (DM) and gas and include self-gravity of gas, stars and DM, radiative cooling, hydrodynamical pressure, shock heating, viscosity, star formation, feedback from evolving stars and type II supernovae, and chemical enrichment as in Mazzei & Curir (2003). We carried out different simulations varying the orbital initial conditions in order to have, for the ideal Keplerian orbit of two points of given masses, the first peri-centre separation, p, equal to the initial length of the major axis of the more massive triaxial halo down to 1/10 of the same axis. For each peri-centre separation we changed the eccentricity in order to have hyperbolic orbits of different energy. The spins of the systems are generally parallel each other and perpendicular to the orbital plane, so we studied direct encounters. Some cases with misaligned spins have

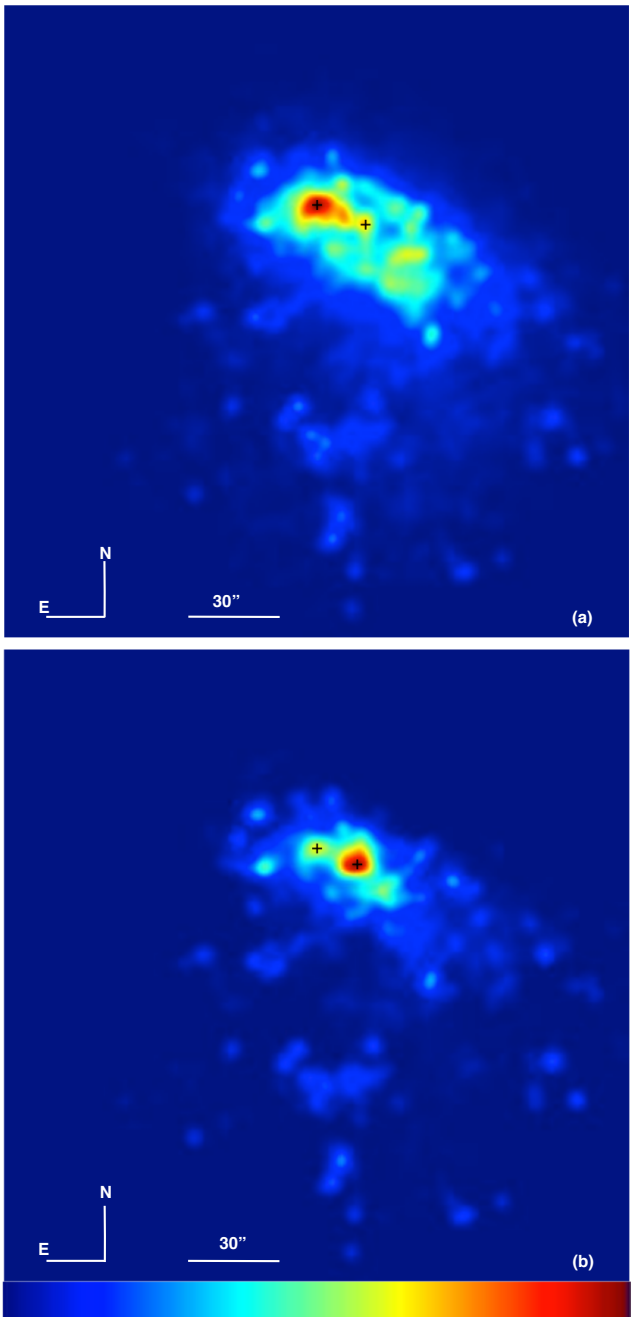

Figure 12. V-band (a) and UV (M2-band, (b)) xz projection of our simulation at the best-fit age; maps are normalized to the total flux within the box, and account for dust attenuation with the same recipes used to provide the SED in Figure 11. The scale is as in Figure 2, with the density contrast being equal to 100. Crosses emphasise the nuclei of the merging galaxies, corresponding to E and Irr in Figure 2 and N-E directions are given to guide the comparison.

Table 5. Input parameters of SPH-CPI simulation of NGC 454

N_{part}	a [kpc]	p/a	r_1 [kpc]	r_2 [kpc]	v_1 [km/s]	v_2 [km/s]	M_T [$10^{10}\,M_\odot$]	f_{gas}
60000	1014	1/3	777	777	57	57	400	0.1

Columns are as follows: (1) total number of initial (t=0) particles; (2) length of the semi-major axis of the halo; (3) peri-centric separation of the halos in units of the semi-major axis; (4) and (5) distances of the halo centres of mass from the centre of mass of the total system, (6) and (7) velocity moduli of the halo centres in the same frame; (8) total mass of the simulation; (9) initial gas fraction of the halos.

been also analysed in order to investigate the effects of the system initial rotation on the results. From our grid of simulations we single out the one which simultaneously (i.e., at the same snapshot) accounts for the following observational constrains providing the best-fit of the global properties of NGC 454: i) total absolute B-band magnitude within the range allowed by observations (see below); ii) the predicted spectral energy distribution (SED hereafter) in agreement with the observed one; iii) morphology like the observed one in the same bands and with the same spatial scale (arcsec/kpc). The results we present are predictions of the simulation which best reproduces all the previous observational constrains at the same snapshot. This snapshot sets the age of the galaxy.

To obtain the SED of the whole system extended over the widest wavelength range, we add to our UV and optical *Swift*-UVOT total fluxes (green points in Figure 11) the B, R and IRAS data (red points in Figure 11) in NED, and the J, H, K total fluxes, derived from 2MASS archive images, which perfectly agree with J, H and K values reported by Tully (2015). All these data are corrected for galactic extinction as reported in §2.2 (Table 3) and §6. The black point in Figure 11 is AKARI/FIS detection. The solid line (red) in Figure 11 highlights the predicted SED.

The simulation which provides this fit corresponds to a major merger between two halos, initially of dark matter and gas, of equal mass and gas fraction (0.1), with perpendicular spins and total mass $4\times10^{12}\,M_\odot$. Their mass centres are initially 1.4 Mpc away each other and move at relative velocity of 120 kms $^{-1}$. Table 5 reports the input parameters of the SPH-CPI simulation best fitting the global properties of the system. The age of the system is 12.4 Gyrs at the best-fit. The far-IR SED accounts for a B-band attenuation of 0.85 mag so that the absolute B-band magnitude of the best-fit snapshot is -21.0 mag. This is the value to be compared with that derived from the distance in Table 1 accounting for an error of ±3.5 Mpc and a total B-band magnitude of 12.66±0.21 mag (from Table 3) , that is M_B=-20.64±0.41 mag.

Our fit of the far-IR emission implies a warm dust component, heated by the UV radiation of H II regions, and a cold component heated by the general radiation field, both including PAH molecules as described in Mazzei et al. (1992, 1994), and Mazzei & Zotti (1994), with a relative contribution, $r_{w/c}$=0.5 which means that 50% of the far-IR emission is due to warm dust emission. The cutoff radius of the cold dust distribution in Figure 11 is $100\,r_c$, r_c being the core radius (Mazzei et al. 1994).

The shape of the far-IR SED suggests the presence of a large amount of dust: the ratio between the the far-IR luminosity and the observed luminosity in the UV to near-IR spectral range is 2.5.

Figure 12 shows the morphology of our simulation at the best-fit age to be compared with that in Figure 2. We point out that the West component dominates the UV morphology and the Est component the optical one, as observed. The simulation shows that these systems will merge within 0.2 Gyr.

Therefore, our approach points towards a picture where E+S pairs can be understood in terms of 1:1 encounters giving rise to a merger in less than 1 Gyr. Of course, this framework deserves further investigation, that is beyond the scope of this work.

8 SUMMARY AND CONCLUSIONS

We used SAM-FP observations at SOAR and *Swift*-UVOT archival images to investigate the kinematical and photometric properties of the NGC 454 interacting/merging system.

According to the definition in Stiavelli et al. (1998), we subdivided the system in NGC 454 E, the early-type member, NGC 454 T, the perturbed area to the North of NGC 454 W, the late-type member, and the two NGC 454 SW and SE complexes South of the late-type. Further subdivision of the NGC 454 W member into W1-W6 have been used to detail single Hα complexes revealed by the monochromatic map (see also Johansson 1988).

We found the following results:

The Hα map shows that the emission is mostly detected in the NGC 454 W system and in the NGC 454SW and NGC 454 SE complexes. A Hα broad emission is revealed in the center of NGC 454 E, with a velocity gradient of 130 km s^{-1} across 4″.

The radial velocity map does not have a rotation pattern neither in the W1-W6 complexes in NGC 454 W, nor in the two SW and SE complexes. W6 shows a velocity gradient of 45 km s^{-1}.

The velocity dispersion map shows that most of the W3-W6, SW and SE complexes have a velocity dispersion in the range 20-25 km s^{-1}. The highest velocity dispersion, 68 km s^{-1} and the lowest, 15 km s^{-1}, are measured in the W1 and W2 complexes, respectively.

We use $(I-\sigma)$ $(I-V)$ $(\sigma-V)$ (see eg. Bordalo et al. 2009) diagnostic diagrams to study the kinematics of the W1-W6 complexes in NGC 454 W and the SW and SE complexes. Diagnostic diagrams show that all regions, except W1 and SW1, have a weak-moderate correlation between the radial velocity and the dispersion interpreted as systematic motions toward or away from the observer. These diagrams

confirm that W1 has high supersonic velocity dispersion and a closer analysis could separate two populations, one in the center with a low dispersion and a second, around it with a higher σ. According to Moiseev & Lozinskaya (2012), W1 could show a Giant HII Region in the center and a turbulent low-density gas cloud in its outskirt. This picture can be discussed further if we take into account the several large profiles in W1 show multiple components. If we only take into account the main component (the brightest), the situation is reversed, with a broader line in the center and narrowed ones around. This can be interpreted as a expanding wind blow bubble according to Lagrois & Joncas (2009).

Based on our SPH simulation with chemo-photometric implementation, the global properties of the system, 12.4 Gyr old, are compatible with an encounter between two halos of equal mass and perpendicular spin. They will merge within 0.2 Gyr. The SED suggests a large FIR emission 2.5 times that in the NUV-NIR range.

The case of NGC 454 system suggests that a class of mixed pairs form via the encounter/merging of similar mass, evolving halos. The different morphologies, emphasized by multi-λ observations, mark a late phase of the merging process.

ACKNOWLEDGEMENTS

Authors would like to warmly thanks A. Tokovinin, C. Mendes de Oliveira and B. Quint to their participation during the run and without which the commissioning of the instrument and the run would not have been possible. Authors would like to thank the anonymous referee for its useful corrections. HP thanks SOAR staff. HP thanks Aix Marseille Université for its financial support during his visit Laboratoire d'Astrophysique de Marseille in April-July 2017. Paola Mazzei and Roberto Rampazzo acknowledge support from INAF through grants PRIN-2014-14 'Star formation and evolution in galactic nuclei' and PRIN-SKA 2016 'Empowering SKA as a probe of galaxy evolution with HI'. We acknowledge the usage of the `HyperLeda` database (http://leda.univ-lyon1.fr). Part of this work is based on archival data, software or online services provided by the ASI SCIENCE DATA CENTER (ASDC). We also acknowledge the usage of the Nasa Extragalactic Database (http://ned.ipac.caltech.edu/) and R free software.

REFERENCES

Amram P., Balkowski C., Boulesteix J., Cayatte V., Marcelin M., Sullivan W. T. III. A&A 1996, 310
Arp, H.C., Madore, B. F. 1987, A Catalogue of Southern Peculiar Galaxies and Associations, Cambridge Univ. Press
Benaglia, T., Chauveau, D., Hunter, D.R., Young, R.S., 2009, Journal of Statistical Software, 32, issue 6
Bordalo, V., Plana, H., Telles, E. 2009, ApJ, 696, 1668
Barton, E.J. 2000, PhD thesis, Harvard University
Barton Gillespie, E., Geller, M. J., Kenyon, S. J. 2003, ApJ, 582, 668
Breeveld, A.A., Curran, P.A., Hoversten, E.A, Koch, S., Landsman, W. et al. 2010, MNRAS, 406, 1687
Breeveld, A.A., Landsman, W. Holland, S.T. et al. 2011, in GAMMA RAY BURSTS 2010. AIP Conference Proceedings, 1358, 373
Combes, F., Prugniel, P., Rampazzo, R., Sulentic, J.W. 1994, A&A, 281, 725
de Mello, D. F., Sulentic, J. W., de Souza, R. E., Reduzzi, L., Rampazzo, R. 1996, A&A, 308, 387
de Mello, D.F., Sulentic, J.W., Rampazzo, R. 1995 Astrophysical Letters & Communications, 1995, 31, 325
de Vaucouleurs, G.1948, Ann. Astrophys. , 11, 247
Domingue, D.L., Sulentic, J.W., Xu, C., Mazzarella, J., Gao, Y., Rampazzo, R. 2003, AJ, 125, 555
Donzelli, C.J., Pastoriza, M.G. 2000, AJ, 120, 189
Einasto, M., Tago, E., Saar, E., Nurmi, P., Enkvist, I., Einasto, P., Heinämäki, P., Liivamägi, L. J., Tempel, E., Einasto, J., Martínez, V. J., Vennik, J., Pihajoki, P., 2010, A&A, 522, A92
Elmegreen, B. G.; Kaufman, M., Thomasson, M., 1993, ApJ, 412, 90
Elmegreen, D.M., Kaufman, M., Brinks, E., Elmegreen, B.G., Sundin, M., 1995 ApJ, 453, 100
Epinat, B., Amram, P., Marcelin, M., Balkowski, C., Daigle, O., Hernandez, O., Chemin, L., Carignan, C., Gach, J.-L., Balard, P, 2008, MNRAS, 388, 500
Faber, S. M., Willmer, C. N. A., Wolf, C., Koo, D. C., Weiner, B. J et al. 2007, ApJ665, 265
Font, J., Beckman, J.E., Rosado, M., Epinat, B., Fathi, K. et al. 2011, ApJL, 740, L1
Fraga, L., Kunder, A.; Tokovinin, A. 2013, AJ, 145, 165
Fraley C, Raftery AE. Journal of Statistical Software, 2007,18, 6, 1
Freeman, K.C. 1970, ApJ, 160, 811
Horellou, C., Booth, R. 1997, A&A Supp. Ser., 126, 3
Irwin, J.A., 1994ApJ, 429, 618I
Jedrzejewski, R., 1987, MNRAS, 226, 747
Johansson,I. 1988, A&A, 191, 29
Karachentsev, I.D., 1972, Comm. Spec. Astrophys. Obs. USSR, 7, 1
Karczewski, O. L., Barlow, M. J., Page, M. J., Kuin, N. P. M., Ferreras, I. et al. 2013, MNRAS, 431, 2493
Knapen, J., Querejeta, M. 2015, Galaxies, 3, 220
Lagrois, D., Joncas, G., 2009, ApJ, 691, 1109
Larson, R. B., Tinsley, B. M 1978, ApJ 219, 46
Laval A., Boulesteix J., Georgelin Y. P., Georgelin Y. M., Marcelin M. A&A 1987, 175, 199
Lelli, F., Duc, P-A., Brinks, E., McGaugh, S. 2015, Galaxies, 3, 184
Lin, L., Patton, D. R., Koo, D. C., Casteels, K., Conselice, C. J. et al. 2008, ApJ, 681, 232
Marchese, E., Braito, V., Della Ceca, R., Caccianiga, A., Severgnini, P. 2012, MNRAS, 421, 1803
Markwardt, C. B. 2009, Astronomical Data Analysis Software and Systems XVIII, 411, 251
Marino, A., Rampazzo, R., Bianchi, L., Annibali, F., Bressan, A., et al. 2011, MNRAS, 411, 311
Marino, A., Mazzei, P., Rampazzo, R., Bianchi, L. 2016, MNRAS, 459, 2212
Mazzei, P., Xu, C., de Zotti, G. 1992, A&A, 256, 45
Mazzei, P., de Zotti, G., Xu, C. 1994, ApJ, 422, 81
Mazzei, P., de Zotti, G. 1994, MNRAS, 266, 5
Mazzei, P., Curir, A., 2003 , ApJ, 591, 784
Mazzei, P., Marino, A., Rampazzo, R. 2014, ApJ, 782, 53
Mendes de Oliveira, C., Amram, P., Quint, B., Torres-Flores, S. 2017, in press (DOI: 10.1093/mnras/stx976)
Mendoza-Castrejón, S., Dultzin, D., Krongold, Y., Gonzàlez, J. J., Elitzur, M. 2015, MNRAS, 447, 2437
Moiseev, A.V., Lozinskaya, T. A. 2012, MNRAS, 423, 1831
Morrissay, P., Conrow, T., Barlow, T.A., Small, T., Seibert, M. et al. 2007, ApJS, 173, 682
Muñoz-Tuñón, C., Tenorio-Tagle, G., Castañeda, H. O. 1996, AJ, 112, 1636
Oke 1974, ApJS, 27, 21

Peterson, S.D. 1979, ApJS, 40, 527
Plana, H., Carvalho, M.S, 2017, in preparation
Poole, T. S., Breeveld, A. A., Page, M. J., Landsman, W., Holland, S. T., et al. 2008, MNRAS, 383, 627
Prugniel, Ph., Héraudeau, Ph., 1998, ApJS, 128, 299
Rampazzo, R., Sulentic, J.W. 1992, A&A, 259, 43.
Rampazzo, R., Reduzzi, L., Sulentic, J.W., Madejsky, R. 1995, A&A Supp. Series, 110, 131
Rampazzo, R., Alexander, P., Carignan, C., Clemens, M. S., Cullen, H. et al. 2006, MNRAS, 368, 851
Rampazzo, R., Marino, A., Tantalo, R., Bettoni, D., Buson, L. M. et al. 2007, MNRAS, 381, 245
Rampazzo, R., Annibali, F., Marino, A., Bianchi, L., Bressan, A. et al. 2011, Ap&SS, 335, 201
Rampazzo, R., Panuzzo, P., Vega, O. et al. 2013, MNRAS, 432, 374
Rampazzo, R., D'Onofrio, M., Zaggia, S., Paturel, G., Boselli, A. et al. 2016, From the Realm of the Nebulae to Populations of Galaxies, Astrophysics and Space Science Library, Volume 435, 381, Springer International Publishing Switzerland
Rampazzo, R., Mazzei, P. Marino, A., Uslenghi, M., Trinchieri, G., Wolter, A. 2017, A&A, 602, A97
Reduzzi, L., Rampazzo, R. 1995, Astrophysical Letters & Communications, 30, 1
Roming, P.W. A., Kennedy, T. E., Mason, K. O., Nousek, J. A., Ahr, L. et al. 2005, Space Science Rev., 120, 95
Sérsic, J. L. (ed.) 1968, Atlas de Galaxias Australes (Cordoba, Argentina: Observatorio Astronomico)
Shuder, J. M., Osterbrock, D. E. 1981, ApJ, 250, 55
Smith, M..; Weedman, D. ApJ 1070, 161, 33
Smith, B. J., Struck, C., Hancock, M., Appleton, P. N., Charmandaris, V., Reach, W.T. 2007, AJ, 133, 791
Smith, B. J., Zaragoza-Cardiel, J., Struck, C., Olmsted, S., Jones, K. 2016, AJ, 151, 53
Soares, D. S. L., de Souza, R. E., de Carvalho, R. R., Couto da Silva, T. C. 1995, A&A Supp., 110, 371
Stiavelli, M., Panagia, N., Carollo, M.C. et al. 1998, ApJL, 492, L135
Struck, C. 2011, Galaxy Collisions. Forging New Worlds from Cosmic Crashes, Springer
Surace, J.A., Mazzarella, J., Soifer, B.T., Wehrle, A.E. 1993, AJ, 105, 864
Tanvuia, L., Kelm, B., Focardi, P., Rampazzo, R. Zeilinger, W. W. 2003, AJ, 126, 1245
Tokovinin, A., Cantarutti, R., Tighe, R. et al. 2010, PASP, 122, 1483
Tokovinin, A., Tighe, R., Schurter, P. et al. 2010, Proc. SPIE, 7736, 77363L
Tully, B.R. 2015, AJ, 149, 117
Vega, O., Bressan, A., Panuzzo, P., Rampazzo, R., Clemens, M., Granato, G. L., Buson, L., Silva, L., Zeilinger, W. W. 2010, ApJ, 721, 1090
Xu, C., Sulentic, J.W. 1991, ApJ, 373, 407
van Dokkum, P. G. 2001, PASP, 113, 1420
van Dokkum, P. G. 2005, ApJ, 130, 2647
Zaragoza-Cardiel, J., Font-Serra, J., Beckman, J.E., Blasco-Herrera, J., García-Lorenzo, B. et al. 2013, MNRAS, 432, 998
Zaragoza-Cardiel, J., Beckman, J.E., Font, J., García-Lorenzo, B., Camps-Fariña, A., Fathi, K., James, P.A., Erroz-Ferrer, S., Barrera-Ballesteros, J., Cisternas, M. 2015, MNRAS, 451, 1307

APPENDIX A: THE ENVIRONMENT OF THE NGC 454 SYSTEM

The NGC 454 system is an isolated pair, RR 23, in the Reduzzi & Rampazzo (1995) catalogue. Assuming the distance given in Table 1 we used `Hyperleda` to inspect a box of 4×4 Mpc^2 for possible neighbors of this nearby system. Table A1, which includes the pair members, provides the galaxy identification (col. 1 and col. 2), the right ascension and declination (col.s 3 and 4), the morphological Type (col. 5), the heliocentric velocity (col. 6), the major axis diameter d_{25} (col. 7) and the axial ratio r_{25} (col. 8) at μ_B=25 mag arcsec^2, the position angle (col. 9) and the total B-band apparent magnitude (col. 10).

Most the galaxies in Table A1 are listed in *A Catalogue of Southern Peculiar Galaxies and Associations* (Arp & Madore 1987) where they are recognized either to show peculiar fearures (AM 0058-580 compact galaxy with diametric jets; AM 0102-573 disrupted galaxy + 2 companions; AM 0126-525 ring or galaxy with loop; AM 0126-515 disturbed spiral) or to be pair members (like our NGC 454 system i.e. AM112-554 I/A double + resolved knots)

Figure A1 shows the histogram of the recession velocity distribution (1000 – 6000 km s^{-1}) in an area of 4×4 Mpc^2 around NGC 454 and the spatial distribution in the same area of the nearby galaxies, shown in green in the top panel. The nearby neighbors are disk galaxies either S0s or Spirals according to the classification of `Hyperleda`. The velocity dispersion of these galaxies is 65 km s^{-1}. This value has to be compared with 327^{+12}_{-2} km s^{-1} of NGC 5486, the third rich galaxy association in the nearby Universe (Marino et al. 2016) and with 92 $^{+3}_{-2}$ km s^{-11} of LGG 225 a very loose group discussed in Mazzei et al. (2014). This picture confirms that NGC 454 system is isolated and located in a very poor environment (see also Tully 2015).

This paper has been typeset from a TEX/LATEX file prepared by the author.

Table A1. Galaxies in 4×4 Mpc the NGC 454 system

Ident.	Other Ident. F	RA (2000) [deg.]	D (2000) [deg.]	T	V_h [km s^{-1}]	$logd_{25}$ log[0.1′]	log r_{25}	PA [deg.]	B_T [mag]
ESO113-004	AM 0058-580	1.00950	-57.74830	5.0	3566±67	0.75	0.19	105.5	15.04±0.20
ESO113-009	AM 0102-573	1.08046	-57.37742	10.0	3648±6	0.99	0.54	165.4	16.02±0.20
NGC 454 W	RR 023a	1.23945	-55.40013	-1.0	3626±2	1.22	0.00	...	13.12± 0.20
NGC 454 E	AM 0112-554; RR 023b	1.24025	-55.39714	-2.0	3635±2	1.28	0.38	80.9	13.14±0.20
ESO113-044	...	1.37632	-57.56919	10.0	3616±8	0.67	0.15	53.3	16.99±0.20
PGC005497	AM 0126-525	1.47367	-52.63588	9.0	3450±42	0.92	0.34	92.7	16.78±0.20
NGC0576	AM 0126-515	1.48269	-51.59871	-1.1	3604±39	0.99	0.08	...	14.42±0.19
ESO196-011	...	1.51217	-51.14189	5.8	3634±6	1.25	0.42	12.6	14.47±0.20

For each galaxies the columns provide the following information: (1) the galaxy identification, (2.3) the (J2000) galaxy coordinates, (4) the morphological type, (5) the heliocentric velocity, (6) the log of the length the projected major axis of a galaxy at the isophotal level 25 mag arcsec^{-2} in the B-band, (7) the log of the axis ratio (major axis/minor axis) of the isophote at 25 mag arcsec^{-2} in the B-band , (8) the position angle, and (9) the total apparent B-band magnitude. Data are from `Hypercat`. Other identification are from `NED`.

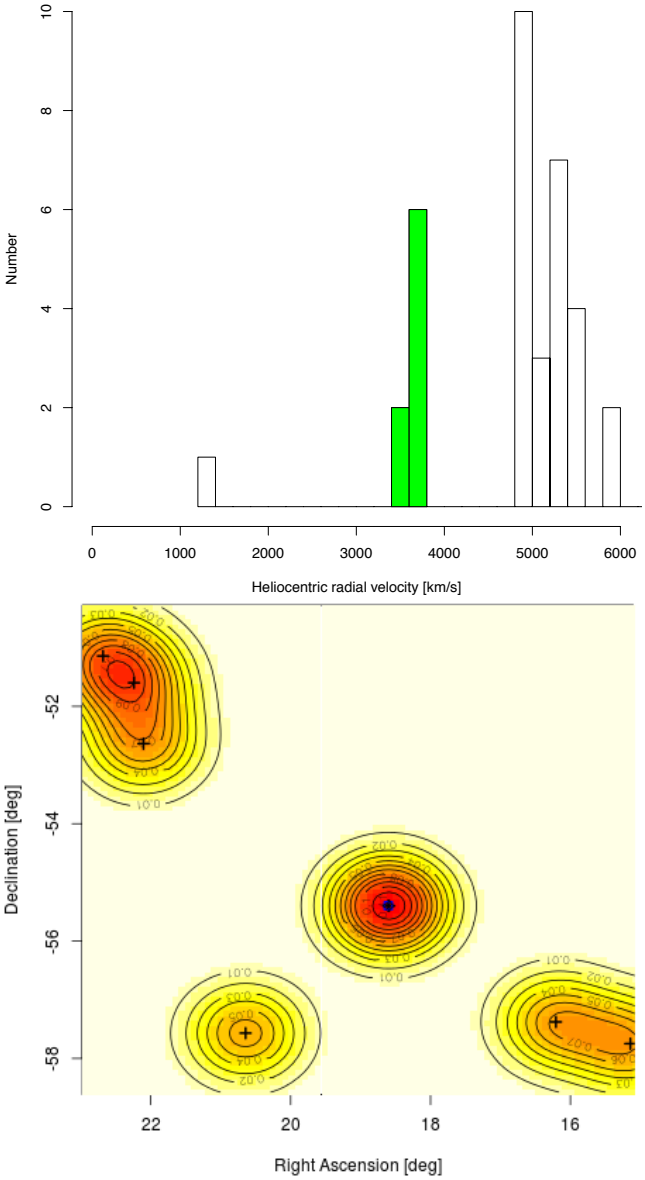

Figure A1. (top panel) Histogram of the heliocentric radial velocity of galaxies within a box of 4×4 Mpc^2 in the range 1000 – 6000 km s^{-1}. (bottom panel) Spatial distribution of galaxies in green in the top panel, i.e. the neighbors of the NGC 454 system. The map is normalized to the total density. Galaxies in the area are listed in Table A1.